

Is the Sun Lighter than the Earth? Isotopic CO in the Photosphere, Viewed through the Lens of 3D Spectrum Synthesis

Thomas R. Ayres

*Center for Astrophysics and Space Astronomy,
University of Colorado, Boulder, CO 80309; email: Thomas.Ayres@Colorado.edu*

J. R. Lyons

Department of Earth and Space Sciences, University of California, Los Angeles, CA

H.-G. Ludwig and E. Caffau

Zentrum für Astronomie der Universität Heidelberg, Heidelberg, Germany

S. Wedemeyer-Böhm

Institute of Theoretical Astrophysics, University of Oslo, Oslo, Norway

ABSTRACT

We consider the formation of solar infrared (2–6 μm) rovibrational bands of carbon monoxide (CO) in CO5BOLD 3D convection models, with the aim to refine abundances of the heavy isotopes of carbon (^{13}C) and oxygen (^{18}O , ^{17}O), to compare with direct capture measurements of solar wind light ions by the *Genesis* Discovery Mission. We find that previous, mainly 1D, analyses were systematically biased toward lower isotopic ratios (e.g., $R_{23} \equiv ^{12}\text{C}/^{13}\text{C}$), suggesting an isotopically “heavy” Sun contrary to accepted fractionation processes thought to have operated in the primitive solar nebula. The new 3D ratios for ^{13}C and ^{18}O are: $R_{23} = 91.4 \pm 1.3$ ($R_{\oplus} = 89.2$); and $R_{68} = 511 \pm 10$ ($R_{\oplus} = 499$), where the uncertainties are 1σ and “optimistic.” We also obtained $R_{67} = 2738 \pm 118$ ($R_{\oplus} = 2632$), but we caution that the observed $^{12}\text{C}^{17}\text{O}$ features are extremely weak. The new solar ratios for the oxygen isotopes fall between the terrestrial values and those reported by *Genesis* ($R_{68} = 530$, $R_{67} = 2798$), although including both within 2σ error flags, and go in the direction favoring recent theories for the oxygen isotope composition of Ca–Al inclusions (CAI) in primitive meteorites. While not a major focus of this work, we derive an oxygen abundance, $\epsilon_{\text{O}} \sim 603 \pm 9$ ppm (relative to hydrogen; $\log \epsilon \sim 8.78$ on the $\text{H} = 12$ scale). That

the Sun likely is lighter than the Earth, isotopically speaking, removes the necessity to invoke exotic fractionation processes during the early construction of the inner solar system.

Subject headings: Line: formation — Molecular processes — Sun: abundances — Sun: infrared — Sun: photosphere

1. Introduction

Isotopic ratios of the abundant light elements, especially carbon and oxygen, chart the history of galactic chemical evolution (Langer & Penzias 1993), and closer to home provide insight into fractionation processes that shaped the primitive solar nebula (Krot et al. 2005). Geochemical mixing models that consider only bulk meteorites and terrestrial planets suggest that (inverse) isotopic ratios of the Sun — expressed as, for example, $^{16}\text{O}/^{18}\text{O}$ — should be only a few tenths of a percent higher than terrestrial standard values¹ (Wiens, Burnett, & Huss 1997), representing an isotopic *deficit* when expressed per mil². Lunar and Martian isotopic ratios are very close to Earth’s; asteroids traced from meteoritic compositions span a wider range, but still deviate from terrestrial by less than 20‰ (Burnett et al. 2003); while comets have a mean ^{13}C deficit of $\sim -45\%$ (Woods 2009). To be sure, some extraterrestrial materials show even larger isotopic deficiencies, reaching -60% for the oxygen isotopes in Ca–Al inclusions (CAI) of chondritic meteorites in the least altered CAIs (Wiens et al. 2004); while some nebular metal grains show isotopic enrichments in the other direction, up to $+180\%$ in the primitive chondrite Acfer 094 (Sakamoto et al. 2007).

One interpretation of the chondritic inclusions led to the prediction that the Sun should be similar to the isotopically lightest CAIs (Clayton 2002). Compositions of solar wind ions implanted in lunar metal grains covered the range from ^{16}O enriched (rare isotopes depleted) and similar to the lightest CAIs (Hahsizume & Chaussidon 2005), to ^{16}O depleted (rare isotopes enhanced), more like atmospheric ozone (Ireland et al. 2006). NASA’s *Genesis* Discovery Mission resolved the conundrum by measuring solar wind isotopes to extremely

¹Based on Vienna Peedee Belemnite [V-PDB] for ^{13}C and the Vienna Standard Mean Ocean Water [V-SMOW] mixture for the oxygen isotopes: Gonfiantini, Stichler, & Rozanski 1995; $^{12}\text{C}/^{13}\text{C}=89.2\pm 0.2$ (ibid., Table 3), $^{16}\text{O}/^{18}\text{O}=498.7\pm 0.1$ (ibid., Table 1), and $^{16}\text{O}/^{17}\text{O}=2632\pm 5$ (ibid., Table 1).

²In the solar system context, isotopic abundances conventionally are reported as differences with respect to the standard terrestrial values in parts per thousand (‰) according to, for example, $\delta^{13}\text{C}_X \equiv [R_{23}^{\oplus}/R_{23}^X] - 1] \times 10^3$, where $R_{23} \equiv \epsilon(^{12}\text{C})/\epsilon(^{13}\text{C})$ is the *inverse* isotopic ratio commonly quoted in solar work (ϵ , for the Sun, is the abundance relative to hydrogen in parts per million [ppm]).

high accuracy through direct capture of the light ions (Burnett et al. 2003). Analysis of *Genesis* collection plates found $\delta^{18}\text{O} = -102.3 \pm 3.3\text{‰}$ and $\delta^{17}\text{O} = -80.8 \pm 5.0\text{‰}$, which implied photospheric values of -59‰ for both isotopes, after accounting for fractionation due to inefficient Coulomb drag during solar wind particle acceleration (McKeegan et al. 2011).

The *Genesis* photospheric values are consistent with the isotopically lightest CAIs, in line with Clayton’s prediction, and imply that a mass-independent fractionation (MIF) process occurred between the Sun and terrestrial planets during solar system formation. Proposed mechanisms for the MIF include CO self-shielding in the solar nebula (Clayton 2002; Lyons & Young 2005); CO self-shielding in the molecular birth cloud (Yurimoto & Kuramoto 2004; Lee, Bergin, & Lyons 2008); galactic chemical evolution of interstellar gas and dust with differing time scales, in this case with the dust younger than the gas (Krot, Nagashima, & Ciesla 2010); and a chemical MIF accompanying O_3 formation in surface reactions on dust grains, which then is imparted to molecular cloud water (Dominguez 2010). Large oxygen isotope effects in CO self-shielding have been measured in at least one molecular cloud (Sheffer, Lambert, & Federman 2002), and in a proto-planetary disk as well (Smith et al. 2009), but with large enough error bars to preclude confirmation of a slope similar to the CAI mixing line.

Spectroscopic determinations of photospheric isotopic abundances offer a different, somewhat contrary, perspective. An early study by Hall, Noyes, & Ayres (1972) of the $2.3\ \mu\text{m}$ $\Delta v = 2$ overtone rovibrational bands of solar carbon monoxide at the McMath-Pierce telescope on Kitt Peak derived a $^{12}\text{C}/^{13}\text{C}$ ratio of 90 with an uncertainty of 15% (at 95% confidence level), consistent with the terrestrial value of 89. The measurements were made in a sunspot, where thanks to the cooler temperatures, the isotopomer transitions attained far greater strength than in the warm photosphere. Overtone transitions of $^{12}\text{C}^{18}\text{O}$ and $^{12}\text{C}^{17}\text{O}$ were not discernible in the $2.3\ \mu\text{m}$ umbral spectrum, however. A follow-up study by Hall (1973) extended the isotopic measurements to the $4.6\ \mu\text{m}$ $\Delta v = 1$ fundamental bands, in the undisturbed photosphere as well as sunspots, using a newly commissioned infrared grating spectrograph at the McMath-Pierce. He derived a slightly lower $^{12}\text{C}/^{13}\text{C}$ ratio of 84 ± 8 , but still consistent with terrestrial. Hall also estimated values for ^{18}O and ^{17}O , again obtaining essentially terrestrial ratios, although with large error bars.

While the CO isotopomer bands are strongly enhanced in sunspots, so too are those of other molecules, leading to complex spectra with substantial line crowding. For this reason, photospheric observations are preferred for the isotope problem, because the warmer temperatures favor durable CO over its more weakly bound cousins like OH and SiO, leading to cleaner, less crowded spectra. Even so, from the ground there are only a few usable

windows in the infrared for the CO measurements, owing to heavy molecular blanketing by the Earth’s atmosphere.

Addressing both these issues, Harris, Lambert, & Goldman (1987) recorded the photospheric CO fundamental bands with a Fourier transform spectrometer (FTS) during a high altitude balloon flight. Adopting the Holweger–Müller (1974) 1D reference temperature stratification (very similar to contemporary 1D semi-empirical models), they derived $^{12}\text{C}/^{13}\text{C} = 84 \pm 5$ and $^{16}\text{O}/^{18}\text{O} = 440 \pm 50$. The $^{12}\text{C}^{17}\text{O}$ spectrum was too weak in their scans to measure. Again, the observed solar ratios were slightly lower than terrestrial, but within the cited uncertainties.

More recently, Ayres, Plymate, & Keller (2006; hereafter APK) analyzed an extensive, high quality record of the solar CO fundamental and first-overtone bands from the Shuttleborne ATMOS FTS, supplemented with ground-based disk center and limb scans obtained with the large 1 m FTS at the McMath-Pierce. The authors synthesized CO line profiles, and center-to-limb behavior, utilizing a variety of 1D photospheric reference models, and multicomponent variants intended to simulate at least the thermal impact of the convective fluctuations that characterize the inhomogeneous solar plasma. Their recommended values of the isotopic ratios were: $^{12}\text{C}/^{13}\text{C} = 80 \pm 1$, $^{16}\text{O}/^{17}\text{O} = 1700 \pm 220$, and $^{16}\text{O}/^{18}\text{O} = 440 \pm 6$, where the cited small uncertainties represented standard errors of the mean (1 s.e.) over the large samples of parent ($^{12}\text{C}^{16}\text{O}$) and isotopic CO transitions considered, but exclusive of possible systematic errors. These ratios, taken at face value, were significantly lower than terrestrial. At the same time, a pioneering study by Scott et al. (2006; hereafter SAGS) of solar CO and the associated isotopomers, again based on the ATMOS material but now using prototype 3D convection models, proposed isotopic ratios $^{12}\text{C}/^{13}\text{C} = 87 \pm 4$ and $^{16}\text{O}/^{18}\text{O} = 480 \pm 30$; higher than APK, slightly lower than terrestrial, but agreeing with both within (2σ) uncertainties.

Notably, while the recent studies found solar $^{12}\text{C}/^{13}\text{C}$ ratios generally consistent with terrestrial, when aggregated together, they all were systematically lower, rather than, say, scattering uniformly around the standard value. Unfortunately, the uncertainties still were too large to distinguish between an isotopically “heavy” versus “light” Sun, especially for ^{18}O and ^{17}O , which as described earlier display a 6% deficit relative to ocean water according to *Genesis*. A more precise measurement of photospheric $^{12}\text{C}/^{13}\text{C}$, as well, might help to distinguish between the several proposed MIF mechanisms. For example, CO self-shielding should initially impart a large depletion of $^{13}\text{C}^{16}\text{O}$ in the solar nebula, yet that would be removed at least partially, and possibly entirely, by subsequent ion-molecule charge exchange reactions between C^+ and CO. The potentially broad range of depletions has yet to be meaningfully constrained by model calculations, so an accurate measurement of the photospheric ratio could provide some needed guidance.

Here we reconsider the solar CO isotopic analysis, in light of a more recent generation of solar 3D models, which now meet key observational tests that the initial complement of convection simulations was less successful matching. We also have taken special precautions, on the one hand to control and narrow the random (mainly observational) uncertainties of the analysis; and on the other to quantify a variety of systematic effects related to the models, and equally so the laboratory molecular line parameters. We stress that we are attempting to perform precision “forensic” spectroscopy of the solar plasma with uncertainties ideally below 1%, in order to compare to the very precise *Genesis* findings (with $\sim 1\%$ quoted errors). To preview our conclusions, that goal was frustrated by lingering uncertainties in the atomic physics (f -value scales) and more subtle aspects of the modelization, even though state-of-the-art 3D convective snapshots were utilized. Nevertheless, we also demonstrate that especially for ^{13}C , but ^{18}O as well, the observational uncertainties can be controlled to the desired level or better, so that in principle future comparisons of higher precision can be carried out, once the external atomic physics and modelization issues are resolved. We also confirm that the 1D spectrum synthesis approach is essentially useless for this particular molecular problem, although to be sure there are other less pathological cases where a careful 1D analysis can produce similar results to a full 3D study (see, e.g., Ayres 2008).

2. Observations

There is a clear advantage of infrared molecular spectra for tracing photospheric isotopic abundances, as noted in Hall, Noyes, & Ayres (1972): the isotopomer and parent ($^{12}\text{C}^{16}\text{O}$) rovibrational transitions are well separated in frequency, ω (in wavenumbers [cm^{-1}]), owing to the large influence of the different molecular weights on the rotational and vibrational properties of the respective diatoms. Isotopic shifts encountered in the electronic spectra of atoms and ions are minuscule in comparison, and usually much smaller than the thermal line width at photospheric temperatures, rendering isolation of the isotopic component rather tricky, if possible at all.

At the same time, obstacles encountered in an isotopic analysis of solar molecular features are myriad. First, the heavy isotopes of C and O have very low abundances and consequently their absorption lines tend to be weak. These will be more influenced by unrecognized blends, especially in telluric contaminated ground-based spectra, than their much stronger $^{12}\text{C}^{16}\text{O}$ counterparts. Second, the strongest isotopomers are fundamental transitions at the peak of the rotational distributions ($J_{\text{low}} \sim 30$), but the equivalent parent $^{12}\text{C}^{16}\text{O}$ lines are too strong to be useful in an abundance study (Hall 1973). Consequently, the isotopic lines must be compared to intrinsically weak parent lines — high excitation transitions in the

case of $\Delta v = 1$ — thereby creating the possibility of biases in the highly temperature sensitive analysis. Finally, historically there have been significant disagreements among proposed oscillator strengths for the “hot” CO bands (see, e.g., APK).

To be sure, many of these challenges have straightforward solutions. For example, the dominant cause of blending in the CO bands are other CO lines, whose frequencies are precisely known and whose relative strengths can be estimated by spectrum synthesis. Thus, minimally contaminated features can be readily identified. Further, in an isotopic analysis, the absolute accuracy of the oscillator strength scale is not as important as the relative precision (e.g., f_{36}/f_{26} , where the subscript is the isotopomer designation: $26 \equiv {}^{12}\text{C}^{16}\text{O}$, and so forth) over the rotational ladder, given that the relative scalings for the isotopomer f -values depend on ostensibly simple atomic physics considerations, and should be calculated consistently even when the absolute parent strengths might be in error. Additionally, one can consider features covering a range of lower level excitation energies, E_{low} , to help identify temperature-dependent trends, which might arise from systematic deviations of the oscillator strengths with $v_{\text{low}} J_{\text{low}}$, which is correlated with E_{low} , or from the solar model itself. Even so, the analysis probably would not be possible if it were not for the existence of very high-quality FTS scans of the average disk center solar spectrum, free of telluric contamination and in the relevant portions of the infrared, from the space-based ATMOS FTS experiment.

2.1. ATMOS

As noted in APK, Shuttle-borne ATMOS was a high-resolution ($\omega/\Delta\omega \sim 150,000$) FTS instrument designed to study trace molecular species in the Earth’s atmosphere backlit by the rising or setting Sun as viewed from low-Earth orbit. Solar reference spectra, obtained from zenith pointings, were free of terrestrial contamination. The instrument recorded a $\sim 0.1 D_{\odot}$ diameter circular region at disk center, which corresponds to $\mu = 1$ for all intents and purposes ($\mu \equiv \cos\theta$, where θ is the heliocentric angle). The best results were obtained from the final ATMOS flight in 1994 November as part of the ATLAS-3 payload (Abrams et al. 1999). The signal-to-noise of those data is extremely high, better than 10^3 ; well suited for a study like the present one, which must dig down to the very weak isotopic features. Based on clean ATMOS CO lines in common to even higher-resolution McMath-Pierce FTS measurements, we adopted a 2 km s^{-1} FWHM Gaussian approximation to the ATMOS instrumental profile to smooth synthetic CO spectra for comparison with observed line shapes. Details concerning the reduction of the dearchived ATMOS scans can be found in the earlier paper (APK).

2.2. Hybridization of ATMOS Spectral Features: $^{12}\text{C}^{16}\text{O}$ $\Delta v = 1$ and $\Delta v = 2$, and the $\Delta v = 1$ Isotopomers

As alluded earlier, the solar CO bands contain large numbers (literally thousands) of absorption lines, many of which, especially $^{12}\text{C}^{16}\text{O}$, are minimally contaminated by extraneous features. Further, because of the modest, smooth change of gf -value and excitation energy along the rotational ladders of each vibrational band, lines of similar rotational numbers in the same band are very similar to one another in absorption strength: spectral clones if you will. Having a large sample of target transitions potentially is a great benefit, especially to help isolate systematics. In contrast, abundance studies based on only a few accessible features — like photospheric atomic oxygen — become more susceptible to accidental blends, distortions in the local continuum level, and NLTE excitation (e.g., Caffau et al. 2008). Synthesizing absorption profiles of hundreds of CO lines is a trivial matter in classical 1D spectral analysis, but is less attractive for 3D work, where each temporal snapshot is equivalent to tens of thousands of 1D problems, and a dozen or more snapshots well separated in time should be considered to ensure an adequate average.

We worked around the tension of wanting to consider as many CO features as possible, but at the same time minimizing the number of transitions to synthesize in 3D, by combining groups of CO lines of similar excitation, wavenumber range, and absorption depth together to yield “hybrid” features. In this way, we could distill the properties, both observational and laboratory, of perhaps a 150 separate absorptions into a smaller, more tractable sample of a few dozen or so, with increased S/N and better defined continuum levels. For this study, we restricted lower level energies to below $18,000\text{ cm}^{-1}$, which characterizes the majority of the measurable isotopomer features. The goal then was to develop a comparison sample of fundamental and overtone parent lines in this energy interval, as well as the isotopic sample itself. Initial line shape synthesis tests suggested that beyond an equivalent width, W_ω , of about 5 mK μ (10^{-3} cm^{-1}), a typical CO $\Delta v = 1$ line begins to saturate, and thus becomes less responsive for an abundance analysis. The saturation limit for $\Delta v = 2$ lines is about twice as high. We thus also applied these respective W_ω cutoffs as part of our line selection criteria.

In practice, the E_{low} and W_ω cuts severely limited the number of suitable $\Delta v = 1$ features that could be “hybridized;” many more $\Delta v = 2$ lines were available, however. This is an important issue because all of the best (i.e., highest S/N) isotopomer features are of the $\Delta v = 1$ type. Ideally, parent lines and the isotopomer counterparts should be compared on as close to the same basis as possible, to avoid potential systematic errors that might creep into the analysis by, say, pitting $\Delta v = 1$ isotopomers against $\Delta v = 2$ parent lines (the overtone oscillator strengths are smaller by a factor of ~ 100). Because of the relative scarcity

of suitable $\Delta v = 1$ target lines — parents typically too strong, isotopomers typically too weak — we were forced to collect them without paying too much attention to the $v_{\text{low}} J_{\text{low}}$ combinations, but rather more closely to E_{low} (the fundamental quantity that controls the number of absorbers through the Boltzmann factor).

We identified suitable lines for hybridization by considering visualizations of all the CO features that satisfied the E_{low} and W_{ω} cutoffs, and did not have another $^{12}\text{C}^{16}\text{O}$ transition with any significant strength whose line center fell within $\sim \pm 10 \text{ km}^{-1}$ of the target line (i.e., not close enough to disrupt the candidate line, given the typical $\sim 4.4 \text{ km s}^{-1}$ line full width at half maximum intensity [FWHM]). The visualizations compared the observed line shape to simulations from the FAL-C 1D model (Fontenla, Avrett, & Loeser 1993), with abundances adjusted (as a function of E_{low} , as described later) to achieve reasonable matches to known clean $^{12}\text{C}^{16}\text{O}$ lines, and separated according to isotopomer. In this way, blends of $^{12}\text{C}^{16}\text{O}$ target lines with, say, weak coincidental isotopic features could be identified. In order to increase the number of potential hybridization candidates, lines were included that were affected in their far wings (beyond $\sim \pm 10 \text{ km s}^{-1}$) by blends, as long as the nearest edge of the blend terminated short of the target absorption, and as long as the local continuum level appeared to be adequately defined in at least one of the wings. The affected parts of the target profile were ignored when the candidates subsequently were coadded. A list of potentially suitable features was compiled in this way.

That list then was parsed into groups of transitions nearby in wavenumber, close in E_{low} , and similar in absorption depth. The hybridization candidates in each group were aligned by Gaussian centroiding, interpolated onto a finely sampled velocity scale (0.5 km s^{-1} steps), and coadded, evenly weighted, ignoring the portion(s) of the line profile previously flagged as corrupted (trimming was limited to velocities outside the $\pm 5 \text{ km s}^{-1}$ span of the line core).

At the same time, the parallel collection of individual molecular parameters also was “hybridized.” The approach was to average the line strengths (gf -values) and the temperature- and wavenumber-dependent components of the absorption — stimulated emission and Boltzmann excitation factors — for a set of discrete temperatures between 4000 K and 5000 K, then fit the resulting average relation with an optimal combination of gf -value and E_{low} (after setting the transition frequency to a weighted mean of the group). Note that the E_{low} for the R- and P-branch transitions of the same J_{low} are the same, as is the statistical weight $g = (2 J_{\text{low}} + 1)$, but in general the oscillator strengths will differ, favoring the R-branch, and the difference increases up the rotational ladder (as illustrated later, in Fig. 1a). The molecular parameters were hybridized for two independent oscillator strength scales, as described next, and for a third scale — $\langle f \rangle$ — which was a straight average of the two.

2.2.1. Oscillator Strengths

We considered two independent oscillator strength scales for the study: Goorvitch (1994: G94), based on experimentally derived transition matrix elements; and Hure & Roueff (1996: HR96), who utilized theoretical electric dipole moment functions. Figure 1a illustrates the dependence of $\Delta v = 1$ and $\Delta v = 2$ oscillator strengths separated by vibrational band, as a function of lower rotational level, J_{low} , as derived from the HR96 dipole matrix elements, and for a version of the G94 f -values taken from the HITEMP section of the HITRAN database³.

We chose the HITRAN CO line strengths, which were derived from the G94 matrix elements, because the HITRAN values are given to higher precision than the original G94 electronic tabulations. However, a detailed comparison of HITRAN to the G94 scale showed that the latter was systematically very slightly higher (by 0.25%), independent of J_{low} , for both fundamental and first overtone; except for the 2–0 band⁴ which showed a much larger shift ($\sim 5\%$), with a strong increase for higher J_{low} in the P branch, but not the R branch. The small systematic offset undoubtedly can be traced to a slightly different numerical value for the combined physical constants that appear in the conversions from matrix elements to Einstein A -values and ultimately f -values; but the larger J_{low} -dependent offset for the 2–0 band likely signals a more significant numerical issue. Ratios of oscillator strengths between neighboring bands (e.g., $[3 - 1] / [2 - 0]$) at the same J_{low} show very systematic behavior. On this basis, the HITRAN 2–0 band appears to be anomalous. We thus corrected the HITRAN 2–0 band to the G94 scale, and adjusted the rest of the HITRAN $\Delta v = 1$ and $\Delta v = 2$ values for the slight deficit mentioned earlier.

Figure 1b compares ratios of the G94 to HR96 oscillator strengths on an expanded scale to illustrate the differences more clearly. The G94 $\Delta v = 1$ f -values are systematically a few percent lower than those of HR96, but independent of vibrational band or rotational number. In contrast, the $\Delta v = 2$ overtone bands tend to have larger oscillator strengths on the G94 scale, at least for the lower vibrational bands, and the deviations relative to HR96 vary strongly and systematically with both vibrational band and rotational number.

Figure 1c compares f -values of $^{13}\text{C}^{16}\text{O}$ to $^{12}\text{C}^{16}\text{O}$ on the G94 and HR96 scales separately.

³see <http://www.cfa.harvard.edu/hitran/>

⁴The vibrational band designation is $v_{\text{up}}-v_{\text{low}}$, where the leading value is the upper vibrational level, the trailing is the lower, and $\Delta v = 1, 2$ for the fundamental and first overtone, respectively. Note, also, that the rotational lines in a given fundamental or overtone band can be in one of two branches: “P” if the upper state J_{up} is one lower than the initial state J_{low} ($\Delta J = -1$); and “R” if the upper state is one higher ($\Delta J = +1$).

The isotopomer strengths are smaller by about 4%, essentially identical on the two scales, and show minimal dependence on v_{low} or J_{low} . A similar deficit is seen for the oxygen isotopes: $^{12}\text{C}^{17}\text{O}$ is down by 2% and $^{12}\text{C}^{18}\text{O}$ by 4%. The consistent behavior between the two oscillator strength scales supports the premise stated earlier that the relative precision of the isotopomer f -values should be better determined than the absolute parent values.

2.2.2. Equivalent Widths

After the hybrid profiles were constructed, equivalent widths were measured. First, a continuum level was established by considering the intensities on either side of, but well away from, line center (in practice, $6 \text{ km s}^{-1} \leq |v| \leq 10 \text{ km s}^{-1}$). An ‘‘Olympic’’ filter (throwing out the two highest and two lowest values) was applied to the collection of (nine) points in each flanking continuum band separately, and the larger of the medians of the two sets of surviving points was adopted as the continuum level. The dispersion of the normalized points in the flanking reference continuum windows served as an empirical estimate of the photometric noise, which later was utilized to assign an uncertainty to the equivalent width according to the FTS noise model of Lenz & Ayres (1992).

The equivalent width, itself, was measured by fitting a Gaussian profile to the normalized intensities within $\pm 5 \text{ km s}^{-1}$ of line center (which now was located very close to zero velocity owing to the initial centroiding of the constituent profiles). Although the solar CO lines display a systematic convective blueshift of around 350 m s^{-1} , the profiles nevertheless are very close to Gaussian in shape (with a FWHM of around 4400 m s^{-1} for the weak fundamental and overtone lines, but C-bisector amplitudes of only a few hundred m s^{-1} [SAGS]). The Gaussian fitting approach was adopted here (and in the previous work of APK) because as applied (later) to the synthesized profiles, it allows the use of a sparsely sampled frequency grid. This is advantageous in the computationally challenged 3D setting.

The initial sample of hybrid features was subjected to an abundance analysis in a representative 3D snapshot using the average oscillator strengths, to derive an ϵ_{O} consistent with the observed equivalent width for each line separately (see below for details). The resulting distributions of inferred ϵ_{O} with both E_{low} and W_{ω} were examined, and any deviants from the expected smooth relations were culled out. The offending hybrids were vetted to see whether one of the constituent lines was anomalous with respect to the others (affected perhaps by an unrecognized non-CO blend), and if eliminating the offending line could improve the behavior. If not, the outlier hybrid was simply discarded. Ultimately, through this iterative, somewhat arbitrary, process a final sample of 36 hybrid parent lines was developed, 10 $\Delta v = 1$ and 26 $\Delta v = 2$, from about 150 input transitions. Table 1

summarizes the constituent lines and final hybrid parameters (for the $\langle f \rangle$ scale). Figure 2a illustrates the procedure for four representative $\Delta v = 1$ hybrids, and Figure 2b similarly for four $\Delta v = 2$ cases. Note in Table 1 that the hybrid designated 1J26 is the trivial case of a single line, because only one suitable $\Delta v = 1$ could be found for the (key) energy range below 7000 cm^{-1} . Also, we caution that the Gaussian parameters (W_ω , FWHM) listed for the individual contributing lines in a hybrid group should be taken only as a guide, especially for those features with distortions in one wing or the other: the continuum level in the pre-coadded profiles is less well defined than for the final hybrid owing to higher photometric noise and the possible influence of intensity deviations, due to blends, outside the line core. This caution particularly extends to the isotopic sample described next.

The hybridization scheme was applied in a similar fashion to $^{13}\text{C}^{16}\text{O}$, $^{12}\text{C}^{18}\text{O}$, and $^{12}\text{C}^{17}\text{O}$ (9, 4, and 4 hybrids, respectively, representing nearly 70 input transitions). For the isotopomers, the Gaussian fitting imposed a fixed FWHM of 4.14 km s^{-1} , as inferred from the average of the measured widths of the higher-S/N $^{13}\text{C}^{16}\text{O}$ hybrids. The apparent decrease with respect to the $\text{FWHM} \sim 4.4 \text{ km s}^{-1}$ of the narrowest parent $\Delta v = 1$ profiles is somewhat more than expected from the influence of the larger molecular weights on the thermal broadening, but the decrease is replicated in the 3D line shapes of the isotopomers. In addition, the Gaussian centroiding step, prior to coadding, was omitted in favor of accepting the laboratory line centers on the ATMOS frequency scale. (An empirical zero-point calibration of the ATMOS velocity scale was determined for each isotopomer separately according to the mean shift of the hybrid lines relative to 1D synthesized profiles, determined in an initial fitting step.) Examples of the isotopomer hybrids are illustrated in Figures 2c ($^{13}\text{C}^{16}\text{O}$), 2d ($^{12}\text{C}^{18}\text{O}$) and 2e ($^{12}\text{C}^{17}\text{O}$). The calculated hybrid line parameters are summarized in Table 2, again for the reference $\langle f \rangle$ scale.

3. Analysis

In overview, our strategy was first to derive an oxygen abundance for a given solar model using the $^{12}\text{C}^{16}\text{O}$ “parent” hybrid line sample, then calculate the isotopic ratios that reproduced the equivalent widths of the weak isotopomer absorptions for that oxygen abundance. This was done in practice by synthesizing the hybrid line equivalent widths for a small set (4–6) of discrete values [of the oxygen abundance, ϵ_{O} ; or scale factors, s_{ISO} , relative to reference isotopic ratios, $(R_{\text{ISO}})_{\text{STD}}$, where $\text{ISO} = 23$, e.g., refers to $^{12}\text{C}/^{13}\text{C}$] spanning the full range of potential sample variation, and then interpolating with the observed W_ω to deduce the corresponding target value (of ϵ_{O} or s_{ISO}). For convenience, we assumed $\epsilon_{\text{C}} = \frac{1}{2} \epsilon_{\text{O}}$, so that the CO concentration effectively becomes quadratically dependent on the oxygen

abundance (see APK for the physical motivation behind this choice).

The derived ϵ_{O} ’s in the first step typically were found to depend systematically on E_{low} (see SAGS; APK), and usually there was an offset between the $\Delta v = 1$ and $\Delta v = 2$ hybrids as well. The abundance gradients and fundamental/overtone shifts could be due to: (1) systematic errors in the f -value relations as a function of $v_{\text{low}}J_{\text{low}}$ (which correlates with E_{low}); or (2) small thermal differences between the 3D convection models and the real Sun in the CO-absorbing layers (the middle photosphere, well above the continuum-forming zone: see APK and Fig. 3b, below). That the *ab initio* 3D models might depart somewhat from the true Sun in the mid-altitudes of the photosphere would not be Earth-shattering, because the underlying simulations typically are purely radiation-hydrodynamic, lacking the small-scale magnetic fields of the true photosphere (Stein 2012), and usually also missing high-frequency acoustic waves (with wavelengths not resolved by the grid spacing in the computational box), which are strongly damped in the outer photosphere (Ulmschneider 1974). Both of these neglected phenomena potentially could produce additional heating there (e.g., Ayres 1975).

We thus also considered slightly perturbed models for which the thermal structure above the continuum-forming layers was systematically raised by a small amount ($\lesssim 100$ K) so that the resulting mean temperature stratification matched that of a semi-empirical 1D reference model. In these temperature-enhanced models, we usually found a significantly different slope of ϵ_{O} against E_{low} , and that the $\Delta v = 1$ and $\Delta v = 2$ samples displayed an opposite offset compared with the baseline. We then imposed an intermediate temperature correction chosen specifically to force the $\Delta v = 1$ and $\Delta v = 2$ samples to agree. In principle, this middling “Goldilocks” solution represents an atmospheric model whose thermal structure is in harmony with respect to the CO fundamental and overtone bands; but, as we show later, the specific temperature correction does depend on the adopted oscillator strength scale.

We pursued this tripartite strategy for the G94 and HR96 CO oscillator strengths separately, to test for potential systematic errors from that source. When calculating the isotopomer hybrid samples, we imposed the specific $\epsilon_{\text{O}}(E_{\text{low}})$ relation inferred for the $\Delta v = 1$ parent hybrids (since all the isotopic lines are of the $\Delta v = 1$ type). We strove to attain as much consistency at each level of the analysis as possible, but also to explore as much of the potential parameter space as was permitted (by other constraints) to judge by how much the final results might be influenced by the models and/or molecular parameters. The individual pieces of the strategy are described in more detail next.

3.1. CO5BOLD 3D Snapshots and Continuum Tests

We adopted the so-called “CO5BOLD” radiation-hydrodynamic (RHD) scheme to provide the baseline 3D models for the CO infrared spectral synthesis. The methodology behind the CO5BOLD 3D stellar convection simulation code has been described by Freytag et al. (2012), who have compared results from this and other contemporary 3D RHD simulations, with excellent agreement achieved for key tests such as visible continuum center-to-limb behavior (see, also, Beeck et al. 2012). Wedemeyer-Böhm & Rouppe van der Voort (2009) have examined photospheric intensity distribution functions in blue, green, and red continuum bands, at disk center and near the limb, from *Hinode* Solar Optical Telescope images (corrected for point response and stray light), and concluded that the CO5BOLD 3D simulations well reproduced the various observables that characterize the granular fluctuation patterns. This agreement gives us confidence for the infrared problem, since the 2.3 μm and 4.6 μm continua bracket the formation depths of the visible radiation.

We utilized sixteen independent 3D snapshots, well separated in time, from a fully-relaxed CO5BOLD run. This is a slightly reduced set of those employed by Caffau et al. (2008) in their analysis of photospheric atomic oxygen: see that study for more modelization details. Figure 3a illustrates schematic temperature and velocity maps for the snapshots collectively, for a constant height slice (median z of the $p = 10^5$ dyne cm^{-2} pressure surface) characteristic of the deep photosphere where the visible continuum arises. There are a dozen, or so, identifiable granules in each snapshot, which have the familiar broad, warm upwelling centers, surrounded by narrower, cool subducting lanes. The area asymmetry largely is responsible for the convective blueshifts seen in most photospheric lines.

Each snapshot has 40 km steps in the two horizontal directions, covering a 5.6×5.6 Mm^2 patch of the surface, and 15 km grid steps in the vertical direction, with an extent of 2.3 Mm; altogether a resolution of $140 \times 140 \times 150$. The top boundary of the snapshots was very high ($< 10^{-6}$ in Rosseland optical depth), well above the CO-absorbing layers in the middle photosphere; and for convenience we truncated the vertical grid at a maximum depth such that $\tau \gg 1$ at any relevant frequency, thus ignoring the deepest layers that are important for the deep-seated granulation dynamics, but not the CO spectrum synthesis confined to the surface layers.

Twelve opacity bins were utilized for the radiation transport in the RHD simulations, a significant improvement over earlier generations of such models that were derived using only one or a few radiative bands. Abundances were taken from Grevesse & Sauval (1998), except for CNO where values closer to Asplund, Grevesse, & Sauval (2005) were adopted. The fact that the 3D time series was calculated with CNO abundances that we later show are inconsistent with what we find from CO is not vital, because: (1) the CNO abundances

are not critical to the model pressure structure (the metals that provide the electrons for the H^- opacity are far more important); and (2), we apply a “calibration” adjustment to the model pressure scales to compensate for any slight such inconsistencies, as outlined next.

As described in a previous 3D study (of [O I] $\lambda 6300$; Ayres 2008), an important practical consideration in utilizing “imported” RHD models is that there might be slight inconsistencies between the opacities and equation of state employed in the original simulation, and the (usually more detailed) ones embedded in a *post facto* spectrum synthesis code. Such inconsistencies could lead, for example, to the prediction of slightly different continuum intensities (say, in the visible) than were inherent in whatever effective temperature constraint was imposed at the lower boundary of the 3D simulation. We mitigated against such inconsistencies by requiring that the full 3D model (consisting of the 16 independent snapshots) successfully predict absolute continuum intensities (see, e.g., APK) over the visible range 0.44–0.68 μm . We forced such agreement by slightly adjusting the pressures in the model by a uniform multiplicative factor. The slight shift of the pressure scale moves the steep part of the deep-photosphere temperature profile, where the visible continuum forms, inward or outward in optical depth space, thereby changing the temperatures where the continuum becomes optically thick, and thus the emergent intensity field. For this particular multi-snapshot CO5BOLD model, the derived scale factor was 1.033: a small correction, to be sure, given the potentially large inconsistencies that in principle could be found in such a comparison. The pressure adjustment has much less impact on the middle photosphere, where the temperatures have flattened out compared to the deeper layers.

Also highlighted in Fig. 3a are three snapshots selected for a more detailed analysis to examine the role of systematic effects, for example arising from the stochastic nature of the independent thermal profiles (i.e., how many snapshots are needed for a reliable average) or from the oscillator strength scales (which have a subtle impact on the “Goldilocks” balance temperatures mentioned earlier). Snapshot “B” has an average upper photospheric temperature profile very similar to that of the full model; snapshot “A” is cooler than average at high altitudes; and snapshot “C” is warmer than average. In general, these temperature deviations are reversed at depth. Also, the pressure scale factor derived from the full 3D model was applied to the individual reference snapshots, rather than deriving a specific scale factor for each, in order to preserve the stochastic intensity fluctuations inherent in such snapshots (although it turned out, by accident, that the three reference snapshots have nearly identical visible continuum intensities, all slightly above the full 3D model).

Figure 3b compares a spatially averaged (on surfaces of constant pressure) version of the full 3D model to the FAL-C semi-empirical 1D stratification. Also shown is the result of applying a uniform temperature shift of +90 K to the outer layers of the 3D model, so

that the pressure-surface average more closely resembles the temperature profile of the semi-empirical model. (We subsequently refer to such a temperature-enhanced 3D model as the “maximally perturbed” scenario, or MAX for short.) The figure includes depth distributions of CO densities, calculated in the models for the same ϵ_{O} (600 ppm), and again averaged on constant pressure surfaces; together with formation depths of the visible continuum ($0.5 \mu\text{m}$), and those at the CO overtone ($2.3 \mu\text{m}$) and fundamental ($4.6 \mu\text{m}$). Although the 1D FAL-C and the MAX variant of the 3D model share the same average $T(p)$ stratification in the CO layers, MAX evidently produces significantly more CO, presumably because the gain in molecular formation in the downward temperature fluctuations more than compensates for the loss in the upward ones. This 1D–3D difference is exaggerated for the CO problem owing to the large, non-linear temperature sensitivity of the molecular chemistry.

Figure 4 illustrates predicted absolute disk center continuum intensities and center-to-limb behavior at $\mu = 0.2$, quite close to the limb, for the three representative snapshots. The underlying observations were described previously in APK, and the 3D continuum synthesis approach in Ayres (2008). In short, Planck functions (thermal emission term) and continuum opacities for each vertical column of the 3D model were interpolated from precalculated tables, according to the local temperature and pressure. Next, the continuum source functions (including Thomson and Rayleigh scattering) were calculated. For simplicity, we implemented a “1.5D”⁵ partial coherent scattering (PCS) formalism, on the native optical depth scale of each vertical column, using the Feautrier-based Hermitian method of Auer (1976). Given the continuum source functions, $S(\tau)$, for each column, 3D specific intensities then were calculated along rays (vertical for disk center, inclined for the limb) according to the formal solution of the transport equation. This was accomplished in practice by interpolating the vertical source functions and opacities onto the rays (which intersect multiple columns for the limb viewing case), and then interpolating the newly derived ray source function onto a fixed optical depth grid, with associated precalculated Feautrier coefficients, to achieve a fast but accurate formal solution for the emergent intensity.

To achieve higher accuracy for the vertical transport calculations, the columns were interpolated onto a finer, 5 km grid. For the limb sightlines, the models were resampled onto a finer, 20 km horizontal grid, and the views from the four cardinal azimuthal directions

⁵1.5D means treating each column of the 3D model as an isolated, laterally homogeneous atmosphere to solve for the angle-dependent radiation fields in the local scattering term. This approximation is valid for the visible continuum, for which the scattering component is small, and the scattering mean-free-paths are short compared to the horizontal variations of the convective structures. In the IR, the approximation is irrelevant, because the scattering term is insignificant, and the source function equals the local Planck function.

($\pm x$, $\pm y$) were averaged (in practice, the differences between the independent views were minimal).

Referring back to Figure 4, there are two sets of center-limb curves depicted. Generally, the lower ones are for the baseline 3D snapshots, while the slightly higher ones are for the temperature-enhanced MAX versions. It is clear that not only do the baseline snapshots reproduce the continuum center-limb behavior reasonably well (and much better than the initial generation of 3D models, which solved the radiation transport utilizing only a few opacity bins), but also the high-altitude temperature perturbation has essentially no influence on the disk center continuum intensities and minimal impact on the center-limb behavior. This is a consequence of restricting the temperature rise to the higher, transparent layers.

We consider the MAX option to be an extreme case, because the contrived match of the mean 3D model to the 1D $T(p)$ profile glosses over important aspects of how spatial averages of different spectral diagnostics feed into the practical construction of a semi-empirical model. Nevertheless, it is encouraging that the simple high-altitude temperature enhancement does not fundamentally violate the “continuum test.” We included the temperature-enhanced snapshots in the CO modeling as a hedge against the possibility that the purely RHD 3D simulations might be slightly too cool in their outer layers, owing to lack of magnetic heating effects and/or damping of high-frequency acoustic waves, as noted earlier. The derived MAX temperature enhancements for the three reference snapshots, treated as independent models, ranged from 75 K (“C”) to 110 K (“A”), with “B” — and the full 3D model — in the middle at 90 K. Under other circumstances these temperature enhancements would be considered minimal, but are significant for the highly temperature-sensitive molecular problem.

3.2. Oxygen Abundances from $^{12}\text{C}^{16}\text{O}$ $\Delta v = 1$ and $\Delta v = 2$

The initial part of the analysis involved utilizing the parent $\Delta v = 1$ and $\Delta v = 2$ hybrid samples to derive the oxygen abundance, and any dependence on excitation energy, over the same range of E_{low} that the strongest isotopomer lines span, as a surrogate for the ideal direct comparison between parent and isotopomer lines of the same $v_{\text{low}}J_{\text{low}}$ (which is not feasible here either due to saturation of the parent lines when the isotopomers are strong, or too weak isotopomers when the parent lines are unsaturated). We emphasize that the main role of the derived oxygen abundance is as a “transfer standard” by which to calibrate the relative isotopic abundances.

As alluded earlier, line shapes of each hybrid transition were synthesized for a set of discrete oxygen abundances, typically four evenly spaced in the log (by 0.03 dex = factor

of 1.07) to span the full range of expected values in that particular snapshot (which varied from model to model, and from unperturbed to MAX). The CO number density was calculated in the instantaneous chemical equilibrium approximation (ICE), again assuming $\epsilon_{\text{C}} = \frac{1}{2} \epsilon_{\text{O}}$, and parsed into the various isotopomer contributions (more details are provided below). Wedemeyer-Böhm et al. (2005) simulated a detailed chemistry network for CO in 2D dynamical models of the photosphere and chromosphere, and concluded that the ICE approximation was accurately obeyed in the dense middle photosphere, where the chemical time scales are very short, although the authors did identify strong departures from equilibrium in the higher, more tenuous layers, especially near chromospheric shock fronts.

The line opacity was determined assuming purely thermal Doppler broadening, compensating for the molecular weight of the particular isotopomer (G94), and shifting the resulting Gaussian profile by the line-of-sight component of the local 3D velocity field (i.e., v_z for the disk center simulations). The line source function was taken to be purely thermal (LTE), an excellent approximation for the middle photosphere where the CO rovibrational collisional rates are very high (Ayres & Wiedemann 1989). The total source function weighted the continuum and line components according to the respective monochromatic opacities.

The line profile was calculated at 26 frequencies. One was a pure continuum point for normalization purposes. The other 25 were distributed symmetrically in velocity: 0.5 km s⁻¹ spacing over the inner ± 5 km s⁻¹ core of the profile, with a few additional points at 1 km s⁻¹ spacing in the line wings. To ease the CO computations, we selected only every other column from the full 3D model, and the three reference snapshots, to carry out the disk center profile synthesis. This is justified because the horizontal sampling of the convective pattern in the CO5BOLD snapshots is, by numerical necessity, much finer than the typical scale lengths of the dominant granular structures.

The equivalent width of each theoretical profile (after smoothing to ATMOS resolution) was measured by a Gaussian fit over the ± 5 km s⁻¹ core of the line (as for the observed features), after compensating for the average convective blueshift. The calculated W_ω versus ϵ_{O} distribution then was modeled by a parabolic function, and the fitted relation was inverted for the observed W_ω to yield the oxygen abundance appropriate to the particular hybrid transition.

This first phase is illustrated in Figures 5a (theoretical and observed profiles) and 5b (abundance fits) for the full 3D model and the average oscillator strengths. Fig. 5a shows that the (smoothed) synthesized profiles very closely match the observed ATMOS hybrid profiles, as was demonstrated by SAGS in more detail for individual CO rovibrational lines (especially by consideration of the C bisectors). The calculated convective blueshifts of the fundamental and overtone lines are about 300 m s⁻¹ and 380 m s⁻¹, respectively, about

half the maximum shifts of weak Fe I and Fe II absorptions in the visible (e.g., Asplund et al. 2000), which tend to form in deeper, more dynamic layers. (The observed profiles were matched to the simulated ones by adjusting the ATMOS frequency scale by a constant velocity offset, separately for $\Delta v = 1$ and $\Delta v = 2$, so that the O–C velocity difference was zero, averaged over all the hybrid transitions of the specific type. The velocity zero point of the ATMOS observations is not known well enough to carry out a direct comparison of observed and calculated convective blueshifts. Furthermore, the CO fundamental and overtone lines form in slightly different layers owing to the displaced continuum “horizons” [see Fig. 3b], so the average convective shifts can be somewhat different.)

The second step in this part of the analysis was to examine the derived $\Delta v = 1$ and $\Delta v = 2$ oxygen abundances (e.g., from Fig. 5b) as a function of excitation energy, E_{low} , and equivalent width, W_ω , to uncover any trends for the particular model. Figure 5c depicts the procedure for the same case illustrated in Figs. 5a and 5b (full 3D model, $\langle f \rangle$ scale). One sees that the derived $\Delta v = 2$ oxygen abundances (in lower portions of the panels) average just below 600 ppm; the ϵ_{O} ’s have a slight but systematic dependence on E_{low} ; the $\Delta v = 1$ and $\Delta v = 2$ samples are separated; but neither group displays a significant trend with equivalent width.

Also included in Fig. 5c are analogous results for the FAL-C 1D model (upper portions of the panels), also using the $\langle f \rangle$ scale, and with all the other assumptions the same (except that a depth-independent microturbulence parameter of 1.7 km s^{-1} was introduced so that the 1D profiles matched the observed line widths). Now, the derived oxygen abundances are much higher (e.g., APK); the excitation slope is much steeper; the $\Delta v = 1$ and $\Delta v = 2$ samples still are separated, and in the same sense as for the 3D model; but also the $\Delta v = 1$ hybrids show increased scatter.

The slope of the ϵ_{O} versus E_{low} distribution was measured by a linear least squares fit to the (more numerous and more diverse in energy) overtone sample, and an offset (specified by the ratio $\rho \equiv \langle \epsilon_{\text{O}} \rangle_{\Delta v=1} / \langle \epsilon_{\text{O}} \rangle_{\Delta v=2}$) was inferred by forcing the (smaller) sample of fundamental lines to fit the same slope. As is clear from the figure, the main dependence is on E_{low} rather than W_ω , consistent with the selection criterion designed to minimize inclusion of partially saturated lines (which would stand out in the W_ω part of the diagram as anomalous). Note that the scatter of individual values about the linear relations is small for the 3D model.

Figure 5d is similar to 5c, but now compares results from the baseline ($\Delta T \equiv 0 \text{ K}$) full 3D model to those of Goldilocks ($\Delta T = 34 \text{ K}$) and MAX ($\Delta T = 90 \text{ K}$), again for the $\langle f \rangle$ scale. The model variants show a systematic increase in ϵ_{O} with ΔT ; a smooth change in the abundance/excitation slope from positive to negative; and a reversal of the $\Delta v = 1$

and $\Delta v = 2$ separation (and, of course, $\rho \equiv 0$ for the Goldilocks option). Significantly, the excitation slope is nearly zero for the Goldilocks case, an outcome that is not a foregone conclusion from simply forcing the $\Delta v = 1$ and $\Delta v = 2$ samples to agree.

Figure 6 summarizes the oxygen abundance exercises for snapshots A–C, provided separately for the independent oscillator strengths, G94 and HR96; the full 3D model for the $\langle f \rangle$ scale; and the 1D model, also for the average f -values.

Although the details differ between the different oscillator strength scales, the overall behavior is similar: the baseline models predict lower oxygen abundances, significant $\epsilon_{\text{O}}/E_{\text{low}}$ slopes, and separated $\Delta v = 1$ and $\Delta v = 2$ distributions (dots mark the $\Delta v = 1$ values), whereas the maximally-perturbed models yield higher oxygen abundances, more negative $\epsilon_{\text{O}}/E_{\text{low}}$ slopes, and $\Delta v = 1$ and $\Delta v = 2$ separated in the opposite sense. The Goldilocks snapshots have intermediate values of ϵ_{O} and intermediate excitation slopes. A subtle consequence of the differences between the G94 and HR96 f -values is on the balance temperatures (the ΔT mentioned earlier) to force $\rho \equiv 0$ for the different models. The G94 scale picks a lower balance temperature, typically closer to the baseline ($\Delta T \equiv 0$), whereas HR96 picks a higher value, closer to the MAX option. Not surprisingly, the average f -value scale selects intermediate balance temperatures. The effect on the balance temperatures is important given the highly temperature sensitive nature of the problem. Also note that the G94 “bow ties” scatter around zero excitation slope, whereas the HR96 symbols appear to be offset from the zero line. This could be taken as some support for the G94 scale over HR96 (although we will see later that other evidence points in the opposite direction).

The $\Delta v = 1$ oxygen abundances of the baseline models (550–580 ppm) are higher than the “low” oxygen abundances (460–490 ppm) derived from atomic oxygen lines initially by Allende-Prieto, Lambert, & Asplund (2001) and subsequently Asplund et al. (2004), which originally inspired the so-called “Oxygen Crisis” conflict with helioseismology (e.g., APK; and references to previous work therein). In fact, the higher values from the “extreme” MAX perturbed snapshots fall around the $\epsilon_{\text{O}} \sim 680$ ppm favored by helioseismology (e.g., Ayres 2008). The Goldilocks values are close to the intermediate ϵ_{O} range proposed in a more recent study of atomic oxygen by Caffau et al. (2008). Again, this comparison assumes that ϵ_{C} is exactly one-half ϵ_{O} : the inferred oxygen abundance would have to be modified to the extent that the true abundance ratio deviates from that value.

The 1D model illustrated here shows a starkly different behavior than the 3D snapshots (as anticipated in SAGS and APK): the inferred ϵ_{O} are much larger, and the excitation slopes are steeper. To the extent that shallow slopes indicate thermal harmony in the models, the 1D example clearly is far away from that ideal; almost certainly because it must represent at each pressure level the wide diversity of temperatures in the real inhomogeneous atmosphere

by only a single compromise value. The spatial averages of ultraviolet and visible spectral diagnostics inherent in forming the 1D model clearly fail miserably to capture the average behavior of the CO $\Delta v = 1$ and $\Delta v = 2$ bands, undoubtedly because the UV/optical has a natural bias toward hotter temperatures, while molecules have the diametrically opposite bias. We can safely conclude that the CO problem is the gold-standard example where a 1D model provides a very misleading — in fact completely useless — viewpoint compared to 3D (as ventured earlier by SAGS).

As a tracer of the oxygen abundance, the CO bands clearly are very model dependent, and thus are more susceptible to systematic errors in the thermal properties of the 3D models than typical atomic lines. Personally we favor the Goldilocks scenario over the unperturbed baseline snapshots, or the MAX variants. We consider the latter to be an extreme case, for the reasons outlined earlier. At the same time, the baseline model very likely is slightly too cool compared with the real photosphere, by virtue of the additional heating process not currently included in the simulations. Thus our natural preference is for the intermediate Goldilocks case: not too cool, not too warm. Our discussion of the oxygen abundance here mainly is for sake of completeness, since we utilize ϵ_{O} essentially as a transfer standard, as cautioned earlier. Thankfully, the rather broad range of derived ϵ_{O} values has a smaller impact on the isotopic analysis, owing to its differential nature (although we will see that part of the anticipated cancellation is not realized owing to the influence of the different f -value scales on the Goldilocks balance temperatures, which feeds back into the isotopic problem).

3.3. Isotopic Ratios

The final piece of the puzzle was to determine the isotopic ratios for the reference snapshots, the full 3D model, and their temperature-perturbed cousins, given the oxygen abundances and excitation slopes derived in the first phase.

Owing to the different molecular weights of the isotopic diatoms, not only are the rovibrational properties different, but so too is the chemistry. The dissociation potential, for example, is slightly affected by the different ground level energies of the isotopomers (Morton & Noreau 1994), as is the kinetic factor in the dissociative equilibrium. Furthermore, the partition functions of each isotopomer are affected by the slightly compressed rovibrational energy ladders (G94).

In the equation of state, we accounted for the ICE formation of the significant diatomic molecules in a solar mixture, based on Grevesse & Sauval (1998) abundances for all elements

except O, which we varied; C, which we took as $\frac{1}{2}$ O; and N, which we set at $\frac{1}{8}$ O. In the ICE solution, for simplicity, we included only the dominant isotope of each element (e.g., ^{12}C for carbon and ^{16}O for oxygen), with the appropriate molecular formation parameters for that combination. This is a good approximation for CO because the contribution by the rare isotopes is only about 1%.

We then treated the CO isotopomer abundances as fractions of the total concentration obtained from the dominant-isotope ICE solution. To derive the relevant ratios, we simulated the full isotopic chemistry, but restricted to CO itself (and the main isotopomers 26, 27, 28, and 36; ignoring the minute concentrations of 37 and 38). We expressed the isotopomer abundance for, say, $^{13}\text{C}^{16}\text{O}$, relative to the calculated total density as

$$n_{36}/n_{\text{CO}} = \gamma_{36} \left[\frac{R_{23}^{-1}}{(1 + R_{23}^{-1})} \right] \left[\frac{1}{(1 + R_{67}^{-1} + R_{68}^{-1})} \right] , \quad (1)$$

where n_{36} is the $^{13}\text{C}^{16}\text{O}$ number density, n_{CO} is the total CO density from the ICE solution, R_{23} is the $^{12}\text{C}/^{13}\text{C}$ ratio, R_{67} is the $^{16}\text{O}/^{17}\text{O}$ ratio, and so forth. The leading term in square brackets simply reflects the fraction of carbon that is ^{13}C , and the trailing term in square brackets reflects the fraction of oxygen that is ^{16}O . The product of the two would be the isotopomer abundance ratio if the chemistry were independent of the molecular weights and dissociation constants. Finally, γ is a correction factor, derived from the CO isotopomer network, which captures the impact of the more subtle chemistry issues. In practice, γ is temperature and density dependent, especially for $T < 4500$ K and high densities ($n_{\text{H}} \gtrsim \text{few} \times 10^{16} \text{ cm}^{-3}$); and exhibits asymptotic behavior below 3500 K and above 5000 K. However, it also happens that the dominant altered factors in the dissociative equilibrium nearly cancel, so γ is close to one, differing from unity at most by only about half a percent in the worst $\{T, n_{\text{H}}\}$ case. That $\gamma \approx 1$ implies that the isotopomer chemistry is close to that of the parent CO, on a per molecule basis, which conveniently justifies the dominant-isotope approximation in the global ICE chemistry.

We calculated the γ 's in detail for medium snapshot ‘‘B,’’ and determined representative values: 1.0010, 1.0007, 1.0016, and 1.000 for isotopomers 36, 28, 27, and 26 respectively. We introduced these as temperature- and density-independent constants in the isotopomer synthesis. This is reasonable because the peak of the CO density function occurs at temperatures much warmer than the low- T limit where the maximum departures of γ from unity occur.

SAGS performed a similar type of analysis, although they also included the factor of the partition function that appears in the line opacity, together with the factor of the partition function in the dissociative equilibrium, because in principle the two cancel, at least if the molecular formation is completely unsaturated (in the sense that $n_{\text{CO}} \sim \epsilon_{\text{C}} \epsilon_{\text{O}} n_{\text{H}}^2$; i.e., only a

small amount of the free carbon and oxygen has associated into CO). We chose to retain the partition function factors explicitly, and separately, in the line opacity and chemical equilibrium to allow for partial saturation effects in the lower temperature overshooting convective plumes of the 3D models, which are not accommodated by the SAGS strategy. Furthermore, the SAGS “opacity scale factors” were derived taking the isotopomer oscillator strengths equal to those of the equivalent parent transitions. However, the isotopomer strengths on either the G94 or HR96 scales are $\sim 4\%$ less than for the equivalent parent transition (for 36 and 28; e.g., Fig. 1c), leading to a systematic error of at least that magnitude (isotopic abundances underestimated, and isotopic ratios, R , overstated), all else being equal.

We adopted reference $(R_{\text{ISO}})_{\text{STD}}$ ’s of 90, 500, and 2650 for $\text{ISO} = 23, 68,$ and $67,$ respectively (essentially the terrestrial standard values); then calculated equivalent widths for multiples (s_{ISO} , as described earlier) of these, from -0.050 dex to $+0.075$ dex, in steps of 0.025 dex (six total). As we did for the oxygen abundances from the parent sample, we fitted a parabolic relation to the calculated equivalent widths and solved for the isotopic ratio scale factor that matched the observed W_{ω} . Figures 7a–c illustrate the procedure for the Goldilocks version of the full 3D model, utilizing the $\langle f \rangle$ scale. We adopted a specific oxygen abundance, $(\epsilon_{\text{O}})_{\text{ref}}$, for each simulation based on the $\Delta v = 1$ sample, but adjusted the oscillator strengths of the isotopomer transitions (all $\Delta v = 1$ type) by a multiplicative factor β to compensate for any slope in ϵ_{O} versus E_{low} :

$$\beta = \left(\frac{c_0}{(\epsilon_{\text{O}})_{\text{ref}}} + \frac{c_1}{(\epsilon_{\text{O}})_{\text{ref}}} \times E_4 \right)^2, \quad (2)$$

where $E_4 \equiv (E_{\text{low}}/10^4)$. The intercept, c_0 , and slope, c_1 , of the linear $\epsilon_{\text{O}}/E_{\text{low}}$ relation initially were derived from the $\Delta v = 2$ sample, but then adjusted to $\Delta v = 1$ according to the ρ factor mentioned earlier; note also that $(\epsilon_{\text{O}})_{\text{ref}} \equiv c_0 + c_1$. The β -scaling of the f -values simulates the effect of a gradient in the oxygen abundance with E_{low} , at least in the regime where the CO formation is unsaturated.

Figure 7c shows that for the full 3D model Goldilocks option, and the average oscillator strengths, the isotopic abundance ratios $^{12}\text{C}/^{13}\text{C}$ and $^{16}\text{O}/^{18}\text{O}$ are slightly higher than terrestrial (by about 2%), with only small random errors due to the dispersion of values within each sample, particularly if we are permitted to describe these as standard errors of the mean. The $^{16}\text{O}/^{17}\text{O}$ ratio is slightly higher still, although now the dispersion among the four independent hybrid points is large, paralleling the large individual uncertainties. The $^{12}\text{C}^{17}\text{O}$ features are extremely weak, and therefore especially susceptible to errors in the local continuum level, so any conclusions drawn from that isotopomer will be much less secure than for the stronger $^{13}\text{C}^{16}\text{O}$ and $^{12}\text{C}^{18}\text{O}$ systems.

The derived isotopic ratios are depicted schematically in Figure 8, as a function of ϵ_{O}

($\Delta v = 1$ values) and the ρ ratio described earlier, for the same set of models illustrated previously in Fig. 6.

On the G94 scale, the isotopic ratios are systematically $\sim 2\%$ lower than those derived from the HR96 scale, for the baseline and MAX models. Going from the baselines to the MAX models, the isotope ratios increase systematically for both oscillator strength scales, by nearly same amount for each: 8% higher for 36 and 10% higher for 28 and 27. The dispersion in R_{ISO} among the reference snapshots is 2–3% for the baselines, and about half that for the MAX variants (undoubtedly because the latter are closer together in temperature than the baselines thanks to the temperature-correction procedure).

On the G94 scale, the $\Delta v = 1$ ϵ_{O} values are systematically $\sim 1\%$ higher than those from the HR96 scale, for the baseline models and the MAX variants, due to the systematically slightly lower G94 $\Delta v = 1$ f -values. For the baseline models, the average ϵ_{O} is about 570 ppm with a $\sim 2.6\%$ snapshot dispersion. For the MAX models, the ϵ_{O} dispersion shrinks to about 1%, again likely because of the temperature confluence effect, but the absolute oxygen abundance rises a dramatic 21% to about 685 ppm. The large increase in the derived oxygen abundance with only a small $\Delta T = 75\text{--}110$ K change from the baseline models demonstrates the strong temperature sensitivity of CO. Note, however, that the rise in the isotopic ratios from baseline to MAX is only about half that of the oxygen abundance itself, demonstrating some significant cancellations in the differential analysis.

Now consider the Goldilocks models that force the $\Delta v = 1$ and $\Delta v = 2$ parent samples to agree in oxygen abundance space. The differences between the results for the two oscillator strength scales are more pronounced, because the systematic offsets between the G94 and HR96 f -values for $\Delta v = 1$ and $\Delta v = 2$ went in opposite directions (at least for the lower vibrational bands that are relevant in this analysis), so the balance temperature to force them into agreement was different. In fact, the HR96 Goldilocks temperatures are closer to the MAX values, averaging 50% of the maximum ΔT 's; while the G94 temperatures are closer to the baselines: only 1 K higher in the case of snapshot “C,” and only 7 K higher for “B.” As before, the dispersions of the isotopic ratios among the three Goldilocks snapshots for a given oscillator strength scale are small ($\lesssim 1\%$), but now the HR96 values are systematically higher by about 5–6% than those for G94. The average oxygen abundances are about 600 ppm for G94 and 630 ppm for HR96, with a small ($\sim 2\%$) dispersion among the snapshots in both cases (although with snapshots “B” and “C” giving nearly identical results, but “A” almost 25 ppm higher).

We now are in a position to recommend isotopic ratios based on the global analysis. We choose the Goldilocks option as our preferred temperature correction, because these are the models that achieve agreement between the $\Delta v = 1$ and $\Delta v = 2$ bands. This would be the

desired outcome for a model that has an optimum thermal structure as far as the molecules are concerned, if the oscillator strength scale is reliable. We chose recommended values from the full 3D model, and the average f -values, because we have no reason (yet) to prefer one of the oscillator strength scales over the other. Further, within the set of reference snapshots we can identify the sources of uncertainty devolving from: (1) the reference $\Delta v = 1$ oxygen abundances (small, contributed by the ρ parameter derived from the ten $\Delta v = 1$ hybrids); (2) “noise” in the isotopomer hybrid line samples (generally small, except for isotopomer 27); (3) variations among the snapshots (also small, when considering the full set of 16); and (4) differences imposed by the alternative oscillator strength scales (dominates the others). The first three sources can be characterized by standard errors of the mean, because we are comparing multiple realizations of ostensibly similar objects. For the oscillator strength scales, we have only two examples, so we quote the uncertainty as one-half the difference between the alternative results (equivalent to a 1σ dispersion for a sample of two).

In addition, we can characterize the further uncertainty that arises from the reality that we do not know, *a priori*, which is the more correct 3D model scenario: baseline, Goldilocks, or MAX. This error must be treated as a standard deviation, because we are comparing ostensibly different objects. The derived “scenario uncertainty” typically is larger than any of the individual sources, and in fact is larger than all those collectively (quadratic sum), except again in the case of isotopomer 27, for which the sample random error is large and comparable to the scenario component.

We find:

$^{12}\text{C}/^{13}\text{C} =$	91.4	± 0.5	± 0.3	± 0.2	± 1.2	± 3.0	($\pm 1.3, \pm 3.3$)
$^{16}\text{O}/^{18}\text{O} =$	511	± 3	± 3	± 1.3	± 9	± 21	($\pm 10, \pm 23$)
$^{16}\text{O}/^{17}\text{O} =$	2738	± 16	± 105	± 7	± 50	± 110	($\pm 118, \pm 161$)
$\epsilon_{\text{O}}(\text{ppm}) =$	603	± 2	± 1.3	± 2	± 8	± 28	($\pm 9, \pm 29$)

The first error (1 s.e.) is that associated with the uncertainty of the $\Delta v = 1$ ϵ_{O} applied in the isotopomer synthesis, resulting from scaling the derived $\Delta v = 2$ abundance (which has negligible random error owing to the large number of contributing overtone transitions and their generally small scatter) according to the ρ factor. The $\langle \sigma_{\rho} \rangle \sim 1.2\%$ for the ten $\Delta v = 1$ hybrid lines (1 s.e. $\sim 0.38\%$) is amplified for the isotopic ratios by a factor of ~ 1.6 (derived by numerical experiments). The second uncertainty (1 s.e.) is that due to the isotopomer sample random error (or the $\Delta v = 2$ hybrid sample for ϵ_{O}). The third (1 s.e.) is the snapshot variability, taking the dispersion of results from the three independent reference snapshots, for the $\langle f \rangle$ scale, and dividing by $\sqrt{16}$ to estimate the s.e. over the full 3D model. The

fourth (1σ) is from the f -values, as described above. Finally, the fifth (1σ) is the scenario uncertainty: i.e., which level of temperature correction, if any, should be applied to the baseline model. The leading error quoted in the trailing parentheses is the total uncertainty for the Goldilocks option treated alone, which is the “optimistic” value if we believe that Goldilocks is the most realistic of the scenarios. The second parenthetical error includes the scenario component, and thus would fall at the conservative, pessimistic, end of the uncertainty spectrum. Note that in all cases, the snapshot variability contribution is smaller than the total sample random error (sum of first two terms in quadrature), demonstrating that 16 snapshots is sufficient for the purpose.

Table 3 summarizes abundances and isotopic ratios derived with the three temperature correction scenarios applied to the full 3D model, for the $\langle f \rangle$ scale; and the Goldilocks variants of the full model separately for the G94 and HR96 f -values.

For comparison, we carried out the isotopic analysis using the FAL-C 1D model illustrated earlier. In this case, as with the 3D models, and for all three oscillator strength options, it also was necessary to impose a balance temperature to bring the $\Delta v = 1$ and $\Delta v = 2$ ϵ_{O} ’s into agreement. This ΔT was $\sim +100$ K for the $\langle f \rangle$ scale. Note that because the 1D temperature stratification in a sense already is at the maximum level, owing to the UV/optical bias in its construction, the additional positive temperature enhancement is counterintuitive (and plainly unphysical, to the extent that 1D models can claim to be physical in the first place). Nevertheless, the results from the 1D model follow the pattern seen in 3D: the Goldilocks version yields a higher oxygen abundance than the baseline model by about 13%, while the isotopic ratios also are higher, but only about half of the corresponding ϵ_{O} rise.

The results for the 1D Goldilocks scenario with the average f -values are as follows: $\epsilon_{\text{O}} = 850$ ppm; $^{12}\text{C}/^{13}\text{C}=78.2$; $^{16}\text{O}/^{18}\text{O}=420$; and $^{16}\text{O}/^{17}\text{O}=2195$. Although not directly comparable, these are similar to the 1D values obtained previously by APK, in the sense that the derived isotopic ratios all are significantly lower than terrestrial, while the inferred oxygen abundance is much higher than any contemporary-accepted value. The discouraging corollary is that all the previous efforts devoted to deriving abundances and isotopic ratios from 1D synthesis of CO, and other molecules, must be considered in vain, since it is clear that this particular problem is especially prone to the thermal differences between a 1D average temperature stratification versus the fluctuations inherent in a dynamically convecting late-type photosphere.

To be sure, the earlier Ayres et al. work made a concerted effort to incorporate temperature perturbations in a schematic way by considering a set of 1D multicomponent models that were scaled from a baseline thermal profile by depth-independent positive and negative

increments in temperature, and weighted by a Gaussian-like distribution to mimic observed continuum brightness histograms. However, consideration of the different types of thermal structures populating a 3D snapshot (e.g., Ayres 2008: his Fig. 2), shows that convection does not simply raise and lower the temperature profile uniformly, but rather skews it so that those stratifications that are hot deep in tend to be cooler higher up, and vice versa (origin of the so-called “reversed granulation” pattern at high altitudes). That skewness likely has a fundamental impact on the CO problem, since the continuum forms in deeper layers, while the molecular absorptions form higher up. Furthermore, thanks to the Wedemeyer-Böhm & Rouppe van der Voort (2009) *Hinode* study, we now know that the amplitudes of thermal fluctuations in the photosphere are significantly larger than assumed by APK, who had appealed to ground-based granulation measurements (that apparently were more affected by stray light and the telescope point response profile than realized). Thus, the APK multicomponent strategy was, in effect, much closer to 1D than 3D.

We also note, with respect to the earlier SAGS study, which derived rather lower equivalent values of ϵ_{O} from CO⁶, that the 3D snapshots utilized in that work apparently were somewhat cooler above $\tau_{\text{Ross}} \sim 1$ than those employed here (see, e.g., Caffau et al. 2008, their Fig. 1). The cooler temperature profile likely was a consequence of the fewer-frequency opacity binning used in the earlier models. As we have seen here, cooler mid-photospheric temperatures tend to predict systematically lower oxygen abundances from CO and lower isotopic ratios, all else being equal (although, to be fair, the SAGS isotopic ratios are consistent with those derived here, given the large error bars of the earlier 3D study [Fig. 8]).

4. Discussion and Conclusions

The value $R_{68} = 511 \pm (10, 23)$ [$\delta^{18}\text{O} = -23 \pm 22\text{‰}$] derived from the ATMOS spectra is somewhat smaller of a deficit than the *Genesis* inferred photospheric value of 530 [$\delta^{18}\text{O} = -59$]. Our photospheric R_{67} ratio implies a larger deficit [$\delta^{17}\text{O} = -42 \pm 45\text{‰}$], closer to the *Genesis* result, although hardly any weight can be attached to this owing to the uncomfortably large measurement errors. Therefore our results, while tantalizing, cannot confirm that the solar photosphere falls $\sim 28\text{‰}$ below the terrestrial fractionation line, as determined by *Genesis* (McKeegan et al. 2011). The value of $R_{23} = 91.4 \pm (1.3, 3.3)$ [$\delta^{13}\text{C} = -25 \pm 15$] measured here is similar to our $\delta^{18}\text{O}$ and is slightly higher than the ter-

⁶Although the authors cast their results in terms of the carbon abundance, they did adopt the previous Asplund et al. (2004) low oxygen abundance, and obtained a C/O ratio of about 0.5, consistent with what we use here.

restrial value of 89.2. The main conclusion — given our intermediate modelization strategy and middle choice of oscillator strength scales — is that the photospheric isotopic ratios of carbon and oxygen are slightly on the high side of the terrestrial values, although not to the extent found by *Genesis* for the heavy oxygen isotopes. That the Sun likely is lighter than the Earth, isotopically speaking, means that exotic $\delta > 0$ fractionation mechanisms need not be invoked for the early solar system, although the *Genesis* findings for $\delta^{18}\text{O}$ and $\delta^{17}\text{O}$ imply that whatever the $\delta < 0$ process, it must have been mass-independent (McKeegan et al. 2011).

Taking some additional liberties, we can turn the problem around and ask what are the implications if *Genesis* is correct and the actual photospheric oxygen isotopic ratios are $\sim 60\text{‰}$ above the terrestrial standard values? If we further require that a satisfactory model must have $\rho \sim 1$, we see that this combination favors the HR96 f -value scale (Fig. 8 and Table 3), and by implication $\delta^{13}\text{C} \sim -50$, close to the *Genesis* heavy oxygen deficits; and one step further, an $\epsilon_{\text{O}} \sim 620$ ppm well beyond the upper side of the “low-O” error flags, just at the lower edge of the seismic range.

In short, we reinforce the conclusions of Scott et al. that the solar CO problem is a poster child for the importance of 3D effects: the 1D models simply fail to account for key aspects of the highly temperature sensitive molecular formation, and provide completely misleading results in the end. We showed, moreover, that altering the thermal profiles of the 3D models slightly according to reasonable criteria can achieve a better match to the empirical CO spectra, but with an accompanying significant impact on especially the oxygen abundance. Although we again caution that CO is a less than ideal abundance indicator, and uncertainties remain due to the discordance between the available oscillator strength scales, the derived ϵ_{O} ’s for our favored “Goldilocks” scenario are in accord with the ‘high’ range found in recent 3D studies of solar atomic oxygen, and possibly within striking distance of a value that could be swallowed, without grimacing, by helioseismology.

This work was supported by NSF grant AST-0908293. JRL thanks NASA Origins of Solar Systems and the Penn State Astrobiology Research Center. EC and HGL acknowledge financial support by the Sonderforschungsbereich SFB 881 “The Milky Way System” (subproject A4) of the German Research Foundation (DFG).

REFERENCES

- Abrams, M. C., Goldman, A., Gunson, M. R., Rinsland, C. P., & Zander, R. 1999, *Appl. Opt.*, 35, 2747
- Allende Prieto, C., Lambert, D. L., & Asplund, M. 2001, *ApJ*, 556, L63
- Asplund, M., Grevesse, N., Sauval, A. J., Allende Prieto, C., & Kiselman, D. 2004, *A&A*, 417, 751
- Asplund, M., Grevesse, N., & Sauval, A. J. 2005, *Cosmic Abundances as Records of Stellar Evolution and Nucleosynthesis*, 336, 25
- Asplund, M., Nordlund, Å., Trampedach, R., Allende Prieto, C., & Stein, R. F. 2000, *A&A*, 359, 729
- Auer, L. 1976, *JQSRT*, 16, 931
- Ayres, T. R. 1975, *ApJ*, 201, 799
- Ayres, T. R. 2008, *ApJ*, 686, 731
- Ayres, T. R., Plymate, C., & Keller, C. U. 2006, *ApJS*, 165, 618 (APK)
- Ayres, T. R., & Wiedemann, G. R. 1989, *ApJ*, 338, 1033
- Beeck, B., Collet, R., Steffen, M., et al. 2012, *A&A*, 539, A121
- Burnett, D. S., et al. 2003, *Space Science Reviews*, 105, 509
- Caffau, E., Ludwig, H.-G., Steffen, M., et al. 2008, *A&A*, 488, 1031
- Clayton, R. N. 2002, *Nature*, 415, 860
- Dominguez, G. 2010, *ApJ*, 713, L59
- Fontenla, J. M., Avrett, E. H., & Loeser, R. 1993, *ApJ*, 406, 319
- Freytag, B., Steffen, M., Ludwig, H.-G., et al. 2012, *Journal of Computational Physics*, 231, 919
- Gonfiantini, R., Stichler, W., & Rozanski, K. 1995, IAEA-TECDOC-825 (Vienna: International Atomic Energy Agency), 13
- Goorvitch, D. 1994, *ApJS*, 95, 535 (G94)

- Grevesse, N., & Sauval, A. J. 1998, *Space Science Reviews*, 85, 161
- Grevesse, N., Asplund, M., Sauval, A. J., & Scott, P. 2010, *Ap&SS*, 328, 179 (GASS)
- Hall, D. N. B. 1973, *ApJ*, 182, 977
- Hall, D. N. B., Noyes, R. W., & Ayres, T. R. 1972, *ApJ*, 171, 615
- Harris, M. J., Lambert, D. L., & Goldman, A. 1987, *MNRAS*, 224, 237
- Hashizume, K., & Chaussidon, M. 2005, *Nature*, 434, 619
- Holweger, H., & Müller, E. A. 1974, *Sol. Phys.*, 39, 19
- Hure, J. M., & Roueff, E. 1996, *A&AS*, 117, 561 (HR96)
- Ireland, T. R., Holden, P., Norman, M. D., & Clarke, J. 2006, *Nature*, 440, 776
- Krot, A. N., et al. 2005, *ApJ*, 622, 1333
- Krot, A. N., Nagashima, K., Ciesla, F. J., et al. 2010, *ApJ*, 713, 1159
- Langer, W. D., & Penzias, A. A. 1993, *ApJ*, 408, 539
- Lee, J.-E., Bergin, E. A., & Lyons, J. R. 2008, *Meteoritics and Planetary Science*, 43, 1351
- Lenz, D. D., & Ayres, T. R. 1992, *PASP*, 104, 1104
- Lyons, J. R., & Young, E. D. 2005, *Nature*, 435, 317
- McKeegan, K. D., Kallio, A. P. A., Heber, V. S., et al. 2011, *Science*, 332, 1528
- Morton, D. C., & Noreau, L. 1994, *ApJS*, 95, 301
- Sakamoto, N., Seto, Y., Itoh, S., et al. 2007, *Science*, 317, 231
- Scott, P. C., Asplund, M., Grevesse, N., & Sauval, A. J. 2006, *A&A*, 456, 675 (SAGS)
- Sheffer, Y., Lambert, D. L., & Federman, S. R. 2002, *ApJ*, 574, L171
- Smith, R. L., Pontoppidan, K. M., Young, E. D., Morris, M. R., & van Dishoeck, E. F. 2009, *ApJ*, 701, 163
- Stein, R. F. 2012, *Living Reviews in Solar Physics*, 9, 4
- Ulmschneider, P. 1974, *Sol. Phys.*, 39, 327

- Wedemeyer-Böhm, S., Kamp, I., Bruls, J., & Freytag, B. 2005, *A&A*, 438, 1043
- Wedemeyer-Böhm, S., & Rouppe van der Voort, L. 2009, *A&A*, 503, 225
- Wiens, R. C., Burnett, D. S., & Huss, G. R. 1997, *Lunar and Planetary Institute Conference Abstracts*, 28, 1553
- Wiens, R. C., Burnett, D. S., McKeegan, K. D., Thiemens, M. H., Franchi, I. A., Bochsler, P., & Mao, P. 2004, *Lunar and Planetary Institute Conference Abstracts*, 35, 1296
- Woods, P. M. 2009, arXiv:0901.4513
- Yurimoto, H., & Kuramoto, K. 2004, *Science*, 305, 1763

Table 1. $^{12}\text{C}^{16}\text{O}$ Hybrid Sample

Transition	ω (cm^{-1})	E_{low} (cm^{-1})	gf	W_ω (10^{-3} cm^{-1})	FWHM (km s^{-1})	Flag
2–1 P92	1638.5309	17997.97	1.716×10^{-3}	2.788 ± 0.010	4.44	n
2–1 P91	1644.9269	17666.30	1.702×10^{-3}	3.039 ± 0.010	4.56	n
2–1 P90	1651.3006	17337.83	1.686×10^{-3}	3.178 ± 0.011	4.50	n
2–1 P89	1657.6517	17012.59	1.672×10^{-3}	3.354 ± 0.012	4.51	n
1A26	1648.8911	17464.58	1.683×10^{-3}	3.072 ± 0.005	4.54	
1–0 P94	1648.8738	16683.95	8.841×10^{-4}	2.420 ± 0.013	4.36	n
1–0 P93	1655.3485	16342.62	8.768×10^{-4}	2.614 ± 0.010	4.41	l
1–0 P92	1661.8011	16004.50	8.692×10^{-4}	2.826 ± 0.014	4.50	l
1B26	1655.7844	16321.21	8.733×10^{-4}	2.588 ± 0.004	4.44	
1–0 P90	1674.6395	15337.95	8.543×10^{-4}	3.195 ± 0.012	4.49	n
1–0 P89	1681.0251	15009.55	8.468×10^{-4}	3.363 ± 0.014	4.55	l
1–0 P87	1693.7284	14362.57	8.315×10^{-4}	3.707 ± 0.014	4.61	n
1–0 P86	1700.0458	14044.01	8.239×10^{-4}	3.948 ± 0.019	4.61	l
1C26	1688.8924	14613.11	8.283×10^{-4}	3.538 ± 0.005	4.60	
3–2 P82	1677.9226	16824.71	2.316×10^{-3}	4.219 ± 0.016	4.75	n
4–3 P76	1690.6726	17085.25	2.860×10^{-3}	4.505 ± 0.029	4.83	l
5–4 P71	1696.4065	17725.30	3.330×10^{-3}	4.237 ± 0.021	4.74	r
5–4 P70	1702.2023	17470.95	3.291×10^{-3}	4.513 ± 0.018	4.76	n
1D26	1692.2540	17285.70	2.932×10^{-3}	4.342 ± 0.009	4.80	
2–1 P85	1682.8292	15744.06	1.612×10^{-3}	4.189 ± 0.018	4.68	n
2–1 P84	1689.0661	15435.10	1.596×10^{-3}	4.387 ± 0.019	4.72	n
2–1 P83	1695.2798	15129.43	1.581×10^{-3}	4.458 ± 0.020	4.78	r
2–1 P82	1701.4702	14827.07	1.565×10^{-3}	4.758 ± 0.018	4.79	n
1E26	1692.8647	15250.59	1.579×10^{-3}	4.426 ± 0.009	4.77	

Table 1—Continued

Transition	ω (cm^{-1})	E_{low} (cm^{-1})	gf	W_ω (10^{-3} cm^{-1})	FWHM (km s^{-1})	Flag
9–8 P28	1820.8624	17851.92	2.428×10^{-3}	4.273 ± 0.017	4.65	n
9–8 P22	1847.1185	17308.93	1.930×10^{-3}	4.171 ± 0.013	4.56	n
9–8 P20	1855.6181	17156.12	1.760×10^{-3}	4.183 ± 0.017	4.61	l
1F26	1840.6961	17451.14	2.030×10^{-3}	4.183 ± 0.006	4.63	
8–7 P8	1929.5857	14578.75	6.506×10^{-4}	3.973 ± 0.011	4.47	n
8–7 P7	1933.4265	14549.96	5.704×10^{-4}	3.737 ± 0.016	4.46	r
8–7 R5	1980.2139	14503.17	4.996×10^{-4}	3.628 ± 0.018	4.41	n
8–7 R6	1983.5660	14524.77	5.838×10^{-4}	4.024 ± 0.017	4.46	n
1G26	1955.6292	14541.29	5.761×10^{-4}	3.821 ± 0.007	4.47	
7–6 P5	1966.8906	12518.28	3.639×10^{-4}	4.330 ± 0.016	4.52	n
7–6 P4	1970.6641	12500.11	2.916×10^{-4}	3.797 ± 0.010	4.40	n
7–6 R3	1999.6015	12485.57	2.955×10^{-4}	3.827 ± 0.068	4.39	l
7–6 R4	2003.0602	12500.11	3.701×10^{-4}	4.553 ± 0.020	4.53	b
1H26	1985.3169	12501.79	3.302×10^{-4}	4.115 ± 0.006	4.49	
6–5 P2	2004.1715	10463.23	1.275×10^{-4}	3.493 ± 0.017	4.37	n
5–4 R0	2041.4229	8414.46	5.431×10^{-5}	3.157 ± 0.014	4.33	l
1I26	2021.0742	9539.74	8.641×10^{-5}	3.310 ± 0.009	4.37	
4–3 R0	2067.7353	6350.43	4.415×10^{-5}	4.399 ± 0.023	4.49	n
1J26	2067.7353	6350.43	4.415×10^{-5}	4.399 ± 0.023	4.49	
7–5 P63	3635.1206	17751.86	9.009×10^{-5}	1.067 ± 0.007	4.35	n
7–5 P62	3642.8485	17526.74	8.898×10^{-5}	1.067 ± 0.006	4.23	n
8–6 P54	3652.1604	17807.96	1.074×10^{-4}	1.162 ± 0.009	4.21	r
9–7 P43	3676.6781	17832.96	1.159×10^{-4}	1.259 ± 0.005	4.15	n
9–7 P42	3683.0854	17680.10	1.137×10^{-4}	1.397 ± 0.010	4.36	l

Table 1—Continued

Transition	ω (cm^{-1})	E_{low} (cm^{-1})	gf	W_ω (10^{-3} cm^{-1})	FWHM (km s^{-1})	Flag
2A26	3659.7804	17723.43	1.031×10^{-4}	1.187 ± 0.004	4.28	
8–6 P42	3733.6516	15726.29	8.776×10^{-5}	1.719 ± 0.007	4.05	l
8–6 P41	3740.0303	15575.43	8.605×10^{-5}	1.933 ± 0.007	4.24	r
9–7 P25	3782.1151	15616.62	7.307×10^{-5}	1.649 ± 0.008	4.21	l
9–7 P22	3797.6212	15358.43	6.524×10^{-5}	1.716 ± 0.008	4.34	r
2B26	3761.0750	15576.80	7.796×10^{-5}	1.761 ± 0.004	4.23	
7–5 P34	3833.8782	12627.24	5.481×10^{-5}	2.928 ± 0.006	4.25	n
7–5 P32	3845.6079	12383.19	5.206×10^{-5}	3.104 ± 0.016	4.34	r
7–5 P29	3862.7120	12044.06	4.786×10^{-5}	3.146 ± 0.006	4.21	n
7–5 P25	3884.5963	11642.40	4.207×10^{-5}	3.190 ± 0.008	4.31	l
2C26	3857.0982	12167.44	4.886×10^{-5}	3.072 ± 0.004	4.28	
6–4 P35	3879.0270	10738.94	3.976×10^{-5}	3.807 ± 0.010	4.26	r
6–4 P34	3885.0247	10610.31	3.881×10^{-5}	3.937 ± 0.006	4.27	n
6–4 P33	3890.9573	10485.30	3.784×10^{-5}	3.948 ± 0.010	4.28	r
2D26	3885.0686	10610.17	3.878×10^{-5}	3.850 ± 0.005	4.25	
9–7 R15	3940.7097	14880.83	5.795×10^{-5}	1.778 ± 0.007	4.36	n
9–7 R17	3945.4187	14999.42	6.592×10^{-5}	1.916 ± 0.006	4.31	b
9–7 R18	3947.6644	15064.07	6.999×10^{-5}	1.930 ± 0.009	4.19	l
2E26	3944.7547	14985.55	6.460×10^{-5}	1.855 ± 0.005	4.27	
5–3 P35	3930.2825	8696.96	2.625×10^{-5}	4.456 ± 0.007	4.15	r
5–3 P34	3936.3153	8567.10	2.563×10^{-5}	4.771 ± 0.008	4.26	l
5–3 P33	3942.2830	8440.90	2.499×10^{-5}	4.937 ± 0.008	4.32	l
5–3 P30	3959.7946	8084.27	2.305×10^{-5}	5.472 ± 0.014	4.49	l
5–3 P27	3976.7156	7760.68	2.104×10^{-5}	5.044 ± 0.007	4.26	r

Table 1—Continued

Transition	ω (cm^{-1})	E_{low} (cm^{-1})	gf	W_ω (10^{-3} cm^{-1})	FWHM (km s^{-1})	Flag
5–3 P26	3982.2240	7660.18	2.037×10^{-5}	5.060 ± 0.023	4.25	b
2F26	3955.2330	8189.89	2.337×10^{-5}	4.940 ± 0.006	4.30	
2–0 P50	3985.0994	4862.74	3.360×10^{-6}	2.182 ± 0.008	4.23	n
2–0 P49	3992.1960	4673.53	3.306×10^{-6}	2.325 ± 0.011	4.25	r
2–0 P48	3999.2296	4488.00	3.253×10^{-6}	2.415 ± 0.006	4.26	r
2G26	3992.3851	4669.23	3.303×10^{-6}	2.331 ± 0.007	4.29	
3–1 P42	3988.6813	5563.81	8.922×10^{-6}	4.653 ± 0.009	4.35	n
3–1 P40	4001.7259	5251.07	8.576×10^{-6}	4.575 ± 0.008	4.20	l
3–1 P38	4014.5138	4953.09	8.225×10^{-6}	4.832 ± 0.005	4.23	l
3–1 P36	4027.0438	4669.91	7.863×10^{-6}	4.974 ± 0.013	4.21	l
2H26	4008.8637	5089.47	8.349×10^{-6}	4.701 ± 0.004	4.23	
9–7 R29	3967.5315	16010.58	1.177×10^{-4}	2.349 ± 0.009	4.14	r
9–7 R30	3968.8942	16117.92	1.223×10^{-4}	2.612 ± 0.007	4.33	n
7–5 R61	4081.9755	17305.01	1.724×10^{-4}	2.587 ± 0.009	4.28	l
7–5 R60	4082.9238	17086.66	1.686×10^{-4}	2.850 ± 0.011	4.44	n
2I26	4025.4474	16626.88	1.429×10^{-4}	2.582 ± 0.008	4.30	
7–5 R20	4057.6387	11221.85	4.539×10^{-5}	4.117 ± 0.008	4.29	n
7–5 R22	4061.7586	11379.17	5.031×10^{-5}	4.375 ± 0.016	4.38	l
7–5 R23	4063.7085	11463.29	5.281×10^{-5}	4.346 ± 0.010	4.28	n
2J26	4061.1143	11357.84	4.948×10^{-5}	4.217 ± 0.006	4.29	
7–5 R29	4073.8593	12044.06	6.842×10^{-5}	4.921 ± 0.021	4.54	r
7–5 R33	4079.1405	12503.42	7.945×10^{-5}	4.825 ± 0.009	4.35	n
7–5 R37	4083.2217	13020.18	9.100×10^{-5}	4.831 ± 0.009	4.37	n
2K26	4078.7026	12518.27	7.899×10^{-5}	4.816 ± 0.012	4.41	

Table 1—Continued

Transition	ω (cm^{-1})	E_{low} (cm^{-1})	gf	W_ω (10^{-3} cm^{-1})	FWHM (km s^{-1})	Flag
3–1 P25	4091.2978	3378.95	5.768×10^{-6}	5.746 ± 0.011	4.34	n
3–1 P22	4107.4365	3105.64	5.155×10^{-6}	5.498 ± 0.013	4.24	n
3–1 P18	4128.0192	2794.07	4.309×10^{-6}	5.280 ± 0.012	4.26	l
3–1 P17	4132.9968	2725.63	4.091×10^{-6}	5.173 ± 0.016	4.32	n
2L26	4114.0663	3014.95	4.814×10^{-6}	5.376 ± 0.007	4.28	
6–4 R72	4121.1779	17982.98	1.557×10^{-4}	1.969 ± 0.008	4.27	n
6–4 R70	4124.6822	17470.95	1.495×10^{-4}	2.166 ± 0.013	4.25	l
6–4 R67	4129.3348	16728.00	1.404×10^{-4}	2.508 ± 0.016	4.30	l
2M26	4125.4780	17331.22	1.466×10^{-4}	2.199 ± 0.006	4.27	
6–4 R26	4122.3991	9711.92	4.304×10^{-5}	5.943 ± 0.022	4.30	l
6–4 R28	4125.7047	9914.68	4.680×10^{-5}	6.099 ± 0.012	4.33	n
6–4 R30	4128.7133	10132.02	5.063×10^{-5}	6.116 ± 0.008	4.30	n
6–4 R31	4130.1058	10246.15	5.260×10^{-5}	6.211 ± 0.008	4.34	n
2N26	4126.7659	10003.51	4.816×10^{-5}	6.046 ± 0.006	4.31	
6–4 R36	4135.9451	10871.18	6.273×10^{-5}	6.106 ± 0.008	4.34	n
6–4 R37	4136.8872	11007.03	6.483×10^{-5}	6.110 ± 0.013	4.36	r
6–4 R39	4138.5446	11289.53	6.909×10^{-5}	5.957 ± 0.010	4.33	n
6–4 R40	4139.2596	11436.17	7.126×10^{-5}	5.839 ± 0.008	4.31	n
2O26	4137.6319	11146.33	6.681×10^{-5}	5.984 ± 0.008	4.34	
5–3 R27	4177.5502	7760.68	2.979×10^{-5}	7.307 ± 0.008	4.32	n
5–3 R28	4179.2008	7864.86	3.105×10^{-5}	7.494 ± 0.017	4.39	l
5–3 R29	4180.7772	7972.73	3.232×10^{-5}	7.415 ± 0.005	4.32	n
5–3 R30	4182.2791	8084.27	3.361×10^{-5}	7.483 ± 0.008	4.33	l
5–3 R33	4186.3371	8440.90	3.756×10^{-5}	7.563 ± 0.009	4.37	r

Table 1—Continued

Transition	ω (cm^{-1})	E_{low} (cm^{-1})	gf	W_ω (10^{-3} cm^{-1})	FWHM (km s^{-1})	Flag
5–3 R35	4188.6677	8696.96	4.028×10^{-5}	7.272 ± 0.007	4.31	n
2P26	4182.4733	8136.71	3.391×10^{-5}	7.398 ± 0.006	4.34	
5–3 R69	4181.2480	15240.46	9.776×10^{-5}	2.856 ± 0.009	4.39	n
5–3 R68	4182.7632	14990.39	9.573×10^{-5}	2.963 ± 0.008	4.29	n
5–3 R66	4185.5532	14500.46	9.172×10^{-5}	3.252 ± 0.007	4.31	n
5–3 R65	4186.8282	14260.61	8.976×10^{-5}	3.487 ± 0.020	4.37	l
2Q26	4184.2968	14713.50	9.304×10^{-5}	3.127 ± 0.008	4.34	
4–2 R73	4229.6013	14278.71	6.369×10^{-5}	2.624 ± 0.014	4.49	l
4–2 R72	4231.4032	14012.58	6.240×10^{-5}	2.617 ± 0.007	4.23	l
4–2 R69	4236.3246	13234.62	5.864×10^{-5}	3.034 ± 0.007	4.20	r
4–2 R68	4237.8042	12982.14	5.742×10^{-5}	3.417 ± 0.018	4.43	l
2R26	4234.2155	13559.28	5.967×10^{-5}	2.900 ± 0.008	4.32	
4–2 R27	4231.1521	5683.53	1.777×10^{-5}	8.344 ± 0.013	4.35	l
4–2 R28	4232.8376	5788.69	1.852×10^{-5}	8.422 ± 0.012	4.36	r
4–2 R31	4237.4479	6126.46	2.083×10^{-5}	8.760 ± 0.014	4.43	n
4–2 R32	4238.8355	6246.46	2.162×10^{-5}	8.445 ± 0.008	4.32	n
2S26	4235.0904	5962.72	1.963×10^{-5}	8.472 ± 0.010	4.37	
4–2 R66	4240.5231	12487.48	5.499×10^{-5}	3.959 ± 0.019	4.62	l
4–2 R65	4241.7626	12245.32	5.381×10^{-5}	3.920 ± 0.014	4.40	r
4–2 R64	4242.9224	12006.63	5.263×10^{-5}	4.051 ± 0.008	4.32	n
4–2 R63	4244.0026	11771.41	5.147×10^{-5}	4.180 ± 0.008	4.28	n
4–2 R62	4245.0034	11539.67	5.033×10^{-5}	4.347 ± 0.006	4.26	n
2T26	4242.9628	11984.87	5.235×10^{-5}	4.065 ± 0.009	4.36	
4–2 R35	4242.5487	6628.63	2.405×10^{-5}	8.591 ± 0.015	4.39	l

Table 1—Continued

Transition	ω (cm^{-1})	E_{low} (cm^{-1})	gf	W_ω (10^{-3} cm^{-1})	FWHM (km s^{-1})	Flag
4–2 R36	4243.6361	6763.39	2.488×10^{-5}	8.394 ± 0.008	4.35	n
4–2 R37	4244.6480	6901.83	2.571×10^{-5}	8.295 ± 0.008	4.34	l
4–2 R39	4246.4450	7189.72	2.742×10^{-5}	8.309 ± 0.025	4.43	l
4–2 R40	4247.2298	7339.16	2.830×10^{-5}	7.966 ± 0.025	4.31	r
4–2 R41	4247.9386	7492.25	2.918×10^{-5}	7.966 ± 0.008	4.34	n
2U26	4245.3507	7043.10	2.646×10^{-5}	8.246 ± 0.008	4.37	
3–1 R17	4263.6356	2725.63	5.325×10^{-6}	6.667 ± 0.007	4.27	r
3–1 R18	4266.0904	2794.07	5.657×10^{-6}	6.900 ± 0.011	4.29	n
3–1 R19	4268.4725	2866.29	5.993×10^{-6}	7.101 ± 0.009	4.29	n
3–1 R20	4270.7816	2942.30	6.332×10^{-6}	7.308 ± 0.011	4.28	n
3–1 R21	4273.0177	3022.08	6.675×10^{-6}	7.582 ± 0.017	4.35	l
3–1 R22	4275.1805	3105.64	7.025×10^{-6}	7.641 ± 0.007	4.31	n
3–1 R23	4277.2699	3192.98	7.377×10^{-6}	7.742 ± 0.008	4.31	l
2V26	4270.9033	2958.84	6.333×10^{-6}	7.242 ± 0.006	4.30	
3–1 R82	4265.4063	14827.07	3.812×10^{-5}	1.379 ± 0.008	4.36	n
3–1 R81	4267.9059	14528.02	3.740×10^{-5}	1.408 ± 0.009	4.23	l
3–1 R80	4270.3235	14232.31	3.669×10^{-5}	1.409 ± 0.006	4.03	r
3–1 R78	4274.9127	13650.91	3.528×10^{-5}	1.706 ± 0.012	4.30	l
3–1 R77	4277.0847	13365.25	3.459×10^{-5}	1.767 ± 0.029	4.13	r
2W26	4271.7245	14039.34	3.574×10^{-5}	1.515 ± 0.006	4.19	
3–1 R66	4295.6311	10448.09	2.752×10^{-5}	3.472 ± 0.007	4.26	n
3–1 R65	4296.8351	10203.62	2.692×10^{-5}	3.859 ± 0.010	4.28	n
3–1 R64	4297.9594	9962.65	2.633×10^{-5}	3.759 ± 0.006	4.23	b
2X26	4296.8517	10195.79	2.687×10^{-5}	3.699 ± 0.008	4.27	
2–0 R13	4306.4749	349.69	1.331×10^{-6}	3.975 ± 0.008	4.25	n

Table 1—Continued

Transition	ω (cm^{-1})	E_{low} (cm^{-1})	gf	W_ω (10^{-3} cm^{-1})	FWHM (km s^{-1})	Flag
2–0 R14	4309.2544	403.46	1.436×10^{-6}	4.265 ± 0.016	4.35	l
2–0 R16	4314.5966	522.47	1.648×10^{-6}	4.638 ± 0.007	4.27	n
2–0 R17	4317.1590	587.72	1.757×10^{-6}	4.774 ± 0.013	4.30	r
2Y26	4312.2073	473.25	1.542×10^{-6}	4.387 ± 0.008	4.29	
2–0 R20	4324.4098	806.38	2.089×10^{-6}	5.294 ± 0.009	4.30	n
2–0 R21	4326.6808	886.90	2.203×10^{-6}	5.450 ± 0.015	4.36	r
2–0 R22	4328.8785	971.23	2.318×10^{-6}	5.422 ± 0.006	4.27	n
2–0 R23	4331.0029	1059.37	2.435×10^{-6}	5.508 ± 0.008	4.26	n
2–0 R24	4333.0537	1151.31	2.554×10^{-6}	5.647 ± 0.013	4.29	l
2–0 R25	4335.0309	1247.05	2.673×10^{-6}	5.670 ± 0.007	4.25	n
2Z26	4329.9746	1025.69	2.376×10^{-6}	5.478 ± 0.006	4.29	

Note. — Line center frequencies, ω , and lower level energies, E_{low} , are from G94; gf -values are averages of G94 and HR96. Uncertainties on equivalent widths, W_ω , are 1σ , based on Lenz & Ayres (1992), with an empirical estimate of the photometric noise. Rightmost column (“Flag”) indicates how profile was trimmed before the coaddition step: “n”– no trimming; “l”– left wing trimmed; “r”– right wing; “b”– both wings.

Table 2. Isotopomer Hybrid Sample

Transition	ω (cm^{-1})	E_{low} (cm^{-1})	gf	W_ω (10^{-3} cm^{-1})	FWHM (km s^{-1})	Flag
$^{13}\text{C}^{16}\text{O}$						
2–1 P53	1835.8986	7263.82	1.035×10^{-3}	0.919 ± 0.008	3.97	l
2–1 P52	1841.0593	7074.05	1.017×10^{-3}	1.013 ± 0.007	4.21	n
2–1 P51	1846.1940	6887.74	9.999×10^{-4}	0.986 ± 0.006	4.02	n
1A36	1841.2046	7069.78	1.016×10^{-3}	0.968 ± 0.003	4.14	
5–4 P36	1847.9960	10583.74	1.745×10^{-3}	0.589 ± 0.007	4.08	n
5–4 P32	1866.2495	10098.20	1.564×10^{-3}	0.613 ± 0.011	4.32	r
5–4 P29	1879.6415	9770.51	1.425×10^{-3}	0.650 ± 0.006	4.18	l
5–4 P28	1884.0480	9668.24	1.379×10^{-3}	0.631 ± 0.006	4.08	n
1B36	1869.8756	10022.02	1.518×10^{-3}	0.613 ± 0.004	4.14	
2–1 P45	1876.4530	5842.88	8.935×10^{-4}	1.299 ± 0.010	4.16	r
2–1 P44	1881.4034	5680.97	8.756×10^{-4}	1.272 ± 0.012	4.03	l
1C36	1878.9695	5760.63	8.842×10^{-4}	1.279 ± 0.005	4.14	
2–1 P40	1900.9348	5068.49	8.025×10^{-4}	1.508 ± 0.009	4.25	r
2–1 P37	1915.2963	4646.21	7.468×10^{-4}	1.542 ± 0.011	4.06	l
1D36	1908.3619	4850.57	7.729×10^{-4}	1.514 ± 0.006	4.14	
4–3 P30	1899.3493	7871.16	1.195×10^{-3}	0.934 ± 0.007	4.04	l
4–3 P26	1917.0482	7465.37	1.044×10^{-3}	0.936 ± 0.010	4.01	r
4–3 P23	1930.0159	7198.08	9.289×10^{-4}	0.947 ± 0.006	4.07	n
4–3 P22	1934.2794	7116.07	8.902×10^{-4}	0.957 ± 0.010	4.18	n
1E36	1919.9709	7418.37	1.010×10^{-3}	0.940 ± 0.003	4.14	

Table 2—Continued

Transition	ω (cm^{-1})	E_{low} (cm^{-1})	gf	W_ω (10^{-3} cm^{-1})	FWHM (km s^{-1})	Flag
2–1 P34	1929.4078	4255.87	6.907×10^{-4}	1.646 ± 0.010	4.09	l
2–1 P33	1934.0555	4132.88	6.718×10^{-4}	1.654 ± 0.008	4.05	n
2–1 P30	1947.8280	3785.33	6.145×10^{-4}	1.707 ± 0.009	4.14	n
2–1 P28	1956.8665	3571.53	5.759×10^{-4}	1.787 ± 0.009	4.19	n
2–1 P27	1961.3423	3470.01	5.564×10^{-4}	1.719 ± 0.010	4.14	n
1F36	1946.1313	3838.53	6.188×10^{-4}	1.693 ± 0.005	4.14	
5–4 R27	2080.6760	9569.47	1.522×10^{-3}	0.853 ± 0.007	4.09	l
5–4 R30	2088.1925	9876.26	1.692×10^{-3}	0.863 ± 0.009	4.07	r
5–4 R35	2099.9808	10457.16	1.979×10^{-3}	0.886 ± 0.011	4.26	l
5–4 R37	2104.4344	10713.78	2.095×10^{-3}	0.865 ± 0.008	4.17	l
1G36	2093.1762	10145.43	1.803×10^{-3}	0.850 ± 0.004	4.14	
1–0 R12	2140.8278	286.58	1.469×10^{-4}	1.498 ± 0.036	3.99	r
1–0 R14	2147.2045	385.72	1.702×10^{-4}	1.883 ± 0.010	4.27	l
1–0 R17	2156.5089	561.89	2.053×10^{-4}	1.938 ± 0.029	4.17	l
1–0 R18	2159.5403	627.93	2.171×10^{-4}	1.928 ± 0.042	4.06	l
1H36	2151.8492	480.27	1.847×10^{-4}	1.804 ± 0.005	4.14	
1–0 R42	2221.4090	3301.16	5.117×10^{-4}	2.117 ± 0.009	4.15	n
1–0 R43	2223.5190	3457.45	5.245×10^{-4}	2.109 ± 0.020	4.18	r
1–0 R44	2225.5905	3617.29	5.373×10^{-4}	2.047 ± 0.013	4.15	r
1I36	2223.4707	3455.82	5.241×10^{-4}	2.077 ± 0.010	4.14	
$^{12}\text{C}^{18}\text{O}$						
3–2 P53	1809.5808	9260.84	1.527×10^{-3}	0.167 ± 0.006	4.27	r
3–2 P50	1824.8215	8709.06	1.449×10^{-3}	0.181 ± 0.006	4.36	n

Table 2—Continued

Transition	ω (cm^{-1})	E_{low} (cm^{-1})	gf	W_ω (10^{-3} cm^{-1})	FWHM (km s^{-1})	Flag
3–2 P49	1829.8500	8531.98	1.424×10^{-3}	0.178 ± 0.006	4.86	l
4–3 P42	1840.5850	9401.32	1.628×10^{-3}	0.152 ± 0.008	3.74	n
4–3 P36	1868.8777	8564.81	1.412×10^{-3}	0.169 ± 0.011	4.12	l
1A28	1835.4927	8869.81	1.478×10^{-3}	0.162 ± 0.002	4.14	
1–0 P15	2033.8515	439.11	1.600×10^{-4}	0.300 ± 0.009	4.36	l
1–0 P11	2050.0805	241.59	1.182×10^{-4}	0.238 ± 0.005	4.16	n
1–0 R9	2126.9299	164.74	1.120×10^{-4}	0.237 ± 0.005	3.80	r
1–0 R11	2133.4895	241.59	1.348×10^{-4}	0.332 ± 0.005	4.49	r
1B28	2084.7945	281.80	1.312×10^{-4}	0.268 ± 0.002	4.14	
1–0 R22	2167.0986	925.05	2.637×10^{-4}	0.453 ± 0.006	3.91	b
1–0 R26	2178.2619	1282.61	3.117×10^{-4}	0.512 ± 0.005	4.07	r
1–0 R29	2186.2556	1588.75	3.481×10^{-4}	0.449 ± 0.010	3.82	l
1C28	2177.4391	1272.49	3.067×10^{-4}	0.474 ± 0.004	4.14	
2–1 R37	2179.5029	4632.65	8.799×10^{-4}	0.456 ± 0.012	4.15	r
1–0 R48	2229.1062	4275.82	5.864×10^{-4}	0.376 ± 0.005	4.19	n
1–0 R49	2230.9793	4452.65	5.994×10^{-4}	0.384 ± 0.005	4.33	n
1D28	2209.7509	4472.02	6.878×10^{-4}	0.391 ± 0.002	4.14	
$^{12}\text{C}^{17}\text{O}$						
1–0 P42	1931.5996	3365.44	4.333×10^{-4}	0.056 ± 0.048	4.38	r
1–0 P35	1966.0712	2351.97	3.664×10^{-4}	0.082 ± 0.007	6.71	n
1–0 P34	1970.8816	2221.79	3.569×10^{-4}	0.072 ± 0.008	3.49	l
1A27	1957.6087	2607.09	3.804×10^{-4}	0.058 ± 0.002	4.14	

Table 2—Continued

Transition	ω (cm^{-1})	E_{low} (cm^{-1})	gf	W_ω (10^{-3} cm^{-1})	FWHM (km s^{-1})	Flag
1–0 P50	1890.5340	4740.88	5.074×10^{-4}	0.087 ± 0.006	4.88	n
1–0 P49	1895.7624	4556.38	4.981×10^{-4}	0.027 ± 0.005	2.42	n
2–1 P37	1931.8009	4715.92	7.615×10^{-4}	0.055 ± 0.007	4.02	l
2–1 P34	1946.2171	4318.04	7.040×10^{-4}	0.085 ± 0.004	3.56	n
2–1 P33	1950.9647	4192.67	6.850×10^{-4}	0.068 ± 0.010	2.53	r
3–2 P20	1984.9124	4978.67	6.301×10^{-4}	0.049 ± 0.005	3.49	l
3–2 P16	2001.9015	4706.90	5.081×10^{-4}	0.046 ± 0.006	4.38	l
2–1 R37	2205.3932	4715.92	9.013×10^{-4}	0.063 ± 0.005	2.70	l
1B27	1991.2737	4592.26	6.475×10^{-4}	0.064 ± 0.002	4.14	
2–1 P47	1881.9118	6276.42	9.470×10^{-4}	0.111 ± 0.011	6.46	l
2–1 P42	1907.2048	5451.32	8.554×10^{-4}	0.038 ± 0.005	2.31	l
3–2 P33	1926.3298	6264.26	1.013×10^{-3}	0.080 ± 0.007	8.32	r
3–2 P21	1980.5875	5055.74	6.603×10^{-4}	0.038 ± 0.005	2.30	n
2–1 R42	2216.4885	5451.32	1.028×10^{-3}	0.130 ± 0.011	5.24	b
1C27	2002.3517	5677.56	8.903×10^{-4}	0.058 ± 0.002	4.14	
1–0 P29	1994.4960	1625.94	3.076×10^{-4}	0.066 ± 0.007	3.60	b
1–0 P24	2017.3692	1122.28	2.572×10^{-4}	0.120 ± 0.005	5.44	l
1–0 P21	2030.7301	864.53	2.265×10^{-4}	0.073 ± 0.005	3.67	n
1–0 P15	2056.6177	449.41	1.638×10^{-4}	0.097 ± 0.026	4.88	l
1–0 R7	2145.0538	104.92	9.140×10^{-5}	0.065 ± 0.005	5.48	l
1–0 R9	2151.8983	168.60	1.147×10^{-4}	0.067 ± 0.006	4.25	l
1D27	2052.3259	844.97	1.907×10^{-4}	0.067 ± 0.003	4.14	

Note. — Line center frequencies, ω , and lower level energies, E_{low} , are from G94; gf -values are averages of G94 and HR96. Uncertainties on equivalent widths, W_ω , are

1σ , based on Lenz & Ayres (1992), with an empirical estimate of the photometric noise. Rightmost column (“Flag”) indicates how profile was trimmed before the coaddition step: “n”– no trimming; “l”– left wing trimmed; “r”– right wing; “b”– both wings. A uniform FWHM= 4.14 km s^{-1} was imposed in the Gaussian fitting procedure.

Table 3. Oxygen Abundances and Isotopic Ratios for Full 3D Model

Scenario	ΔT	ϵ_{O}	c_1	ρ	R_{23}	R_{68}	R_{67}
Average f -values							
B	0	572 ± 6	+7	0.972 ± 0.013	$88.9 \pm 0.7 (0.2)$	$493 \pm 7 (3)$	$2642 \pm 204 (102)$
G	+34	603 ± 6	-1	1.000 ± 0.011	$91.4 \pm 0.7 (0.2)$	$511 \pm 9 (4)$	$2738 \pm 209 (104)$
M	+90	644 ± 9	-15	1.050 ± 0.017	$96.2 \pm 0.9 (0.3)$	$544 \pm 10 (5)$	$2915 \pm 203 (101)$
G94 f -values							
G	+17	587 ± 7	+7	1.000 ± 0.014	$89.3 \pm 0.9 (0.3)$	$496 \pm 7 (3)$	$2657 \pm 209 (104)$
HR96 f -values							
G	+51	620 ± 7	-10	1.000 ± 0.010	$93.7 \pm 0.8 (0.3)$	$528 \pm 11 (5)$	$2829 \pm 210 (105)$

Note. — “Scenario” corresponds to one of three temperature correction schemes, parametrized by ΔT (in K): “B” = baseline; “G” = Goldilocks; and “M” = MAX. Abundance gradient, $c_1 = d\epsilon_{\text{O}} / dE_{\text{low}}$, is in units of ppm per 10^4 cm^{-1} . In ϵ_{O} (ppm) and c_1 columns, values refer to $\Delta v = 2$ parent sample; corresponding $\Delta v = 1$ values can be obtained by multiplying by ρ factor. In ϵ_{O} and ρ columns, cited uncertainties are 1σ dispersions. In R_{ISO} columns, first uncertainty is a 1σ dispersion, second is 1 s.e.

Fig. 1.— *(a)* Comparison of two independent oscillator strength scales used in this study: G94 (solid curves) and HR96 (small crosses). The f -values display smooth behavior with J_{low} (negative values refer to P branch, and positive to R), and systematically increase with v_{low} . Truncation of higher $\Delta v = 1$ bands is due to $\omega > 1600 \text{ cm}^{-1}$ cutoff applied to the line samples, corresponding to highest quality ATMOS spectra. *(b)* Similar to *(a)* but showing ratios of G94 to HR96 oscillator strengths on a magnified scale. Slight “noise” in the ratios is due to finite precision in tabular values of G94 oscillator strengths; HR96 values were calculated from smooth analytic functions. G94 fundamental bands ($\Delta v = 1$) are systematically lower by a few percent, without much dependence on v_{low} or J_{low} . In contrast, G94 overtone bands mostly are higher, and the deviations depend strongly on both v_{low} and J_{low} . *(c)* Similar to *(b)* but showing ratios of isotopomer 36 to parent 26 for both oscillator strength scales. Offsets are identical for G94 and HR96, and nearly independent of v_{low} and J_{low} . Similar behavior is seen for the other isotopomers: 28 systematically lower than 26 by about 4%, 27 lower than 26 by about 2%.

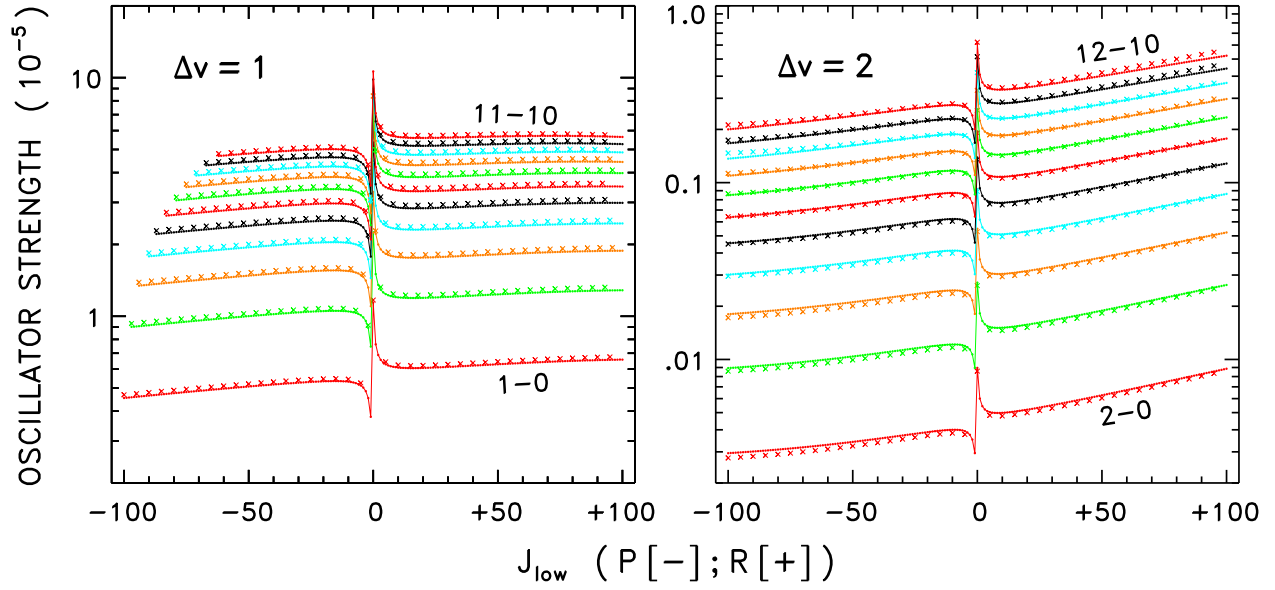


Fig. 1a.—

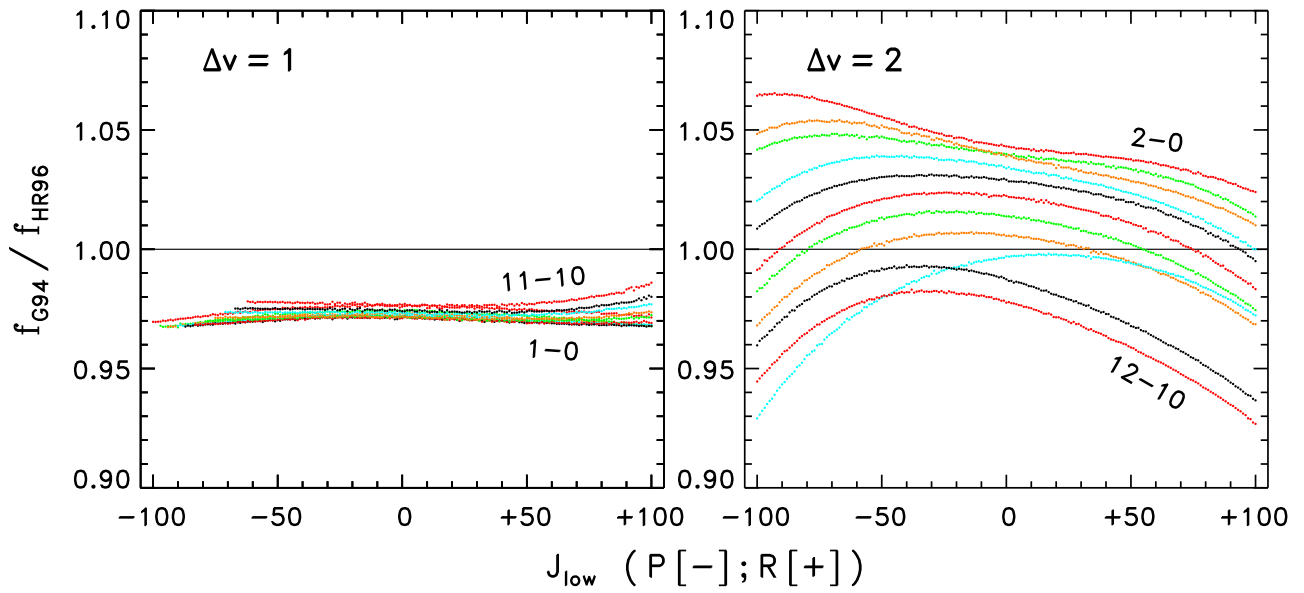


Fig. 1b.—

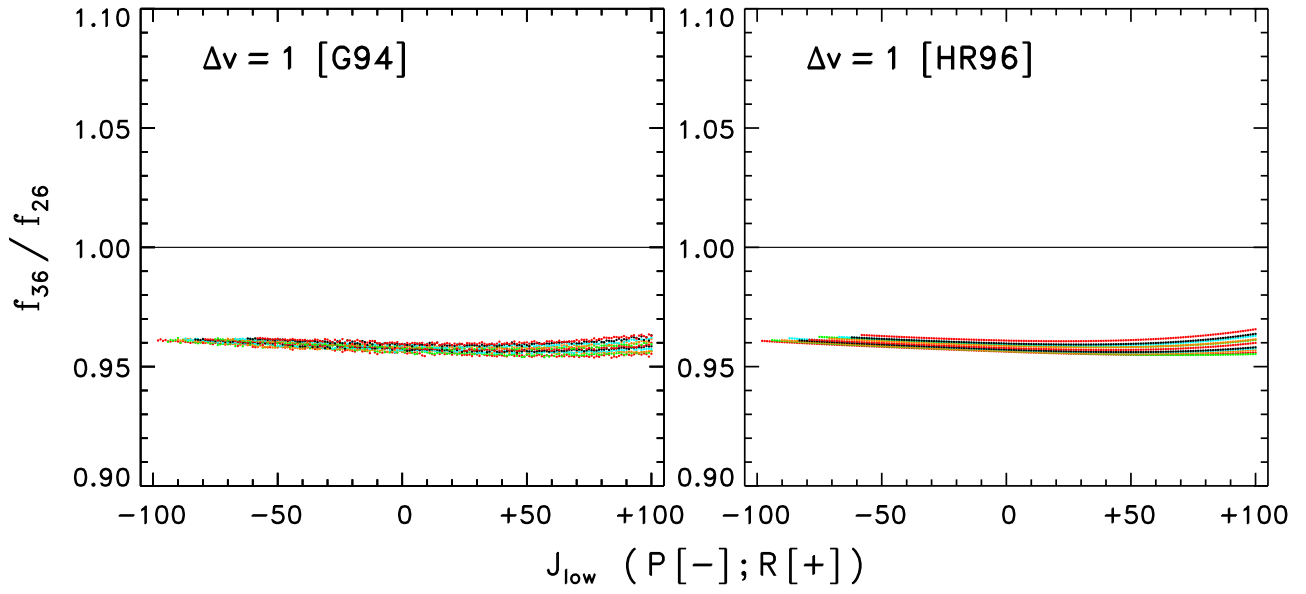


Fig. 1c.—

Fig. 2.— (a) Hybridization of $^{12}\text{C}^{16}\text{O}$ rovibrational lines from ATMOS spectra, for four representative $\Delta v = 1$ transitions. In upper right hand corner of each panel, leading numerical designation in blue is for Δv (1= fundamental; 2= first overtone) followed by letter indicating the transition (cross-referenced to Table 1). Trailing number in red is the isotopomer designation. Below the hybrid line specification is a list of individual transitions that were coadded. These are depicted in the spectral sub-panel at left by thin curves. If colored red, that part of the line profile was ignored in the coaddition. Sum is indicated by solid dots, and underlying thick blue curve is a similar coaddition of isotopomer 26 synthetic spectra calculated from a 1D model but with line oscillator strengths adjusted to compensate for the large gradient in ϵ_{O} with E_{low} found with such models. The synthetic curves were combined without trimming to illustrate corruption to the hybrid line shape that could have occurred. In the lower parts of the panels, temperature-dependent factors for the line opacities (not including n_{CO}) are shown by thin curves (of various colors), and the average at discrete temperatures by large blue dots. Mean of the G94 and HR96 f -values was used for the input line strengths. Red dot-dashed curve is a fit that optimizes values of E_{low} and gf , for the weighted transition frequency, $\langle \omega \rangle$. (b) Same as (a) but for selected $\Delta v = 2$ transitions. (c) Same as (a) but for selected $\Delta v = 1$ $^{13}\text{C}^{16}\text{O}$ transitions. Thick green curves are synthetic spectra for this isotopomer (36), and (wing) blends due to isotopomer 26 (blue) are present in some cases. Negative slope for low-excitation transition 1H36 is caused by the stimulated emission factor. (d) Same as (a) for $\Delta v = 1$ $^{12}\text{C}^{18}\text{O}$ transitions. Thick red curves are synthetic spectra for this isotopomer (28), and (wing) contributions from other isotopomers can be seen as well. (e) Same as (a) for $\Delta v = 1$ $^{12}\text{C}^{17}\text{O}$ transitions. Thick orange curves are synthetic spectra for this isotopomer (27). Blending by other isotopomers is particularly conspicuous since the $^{12}\text{C}^{17}\text{O}$ line depths are only a few tenths of a percent at best.

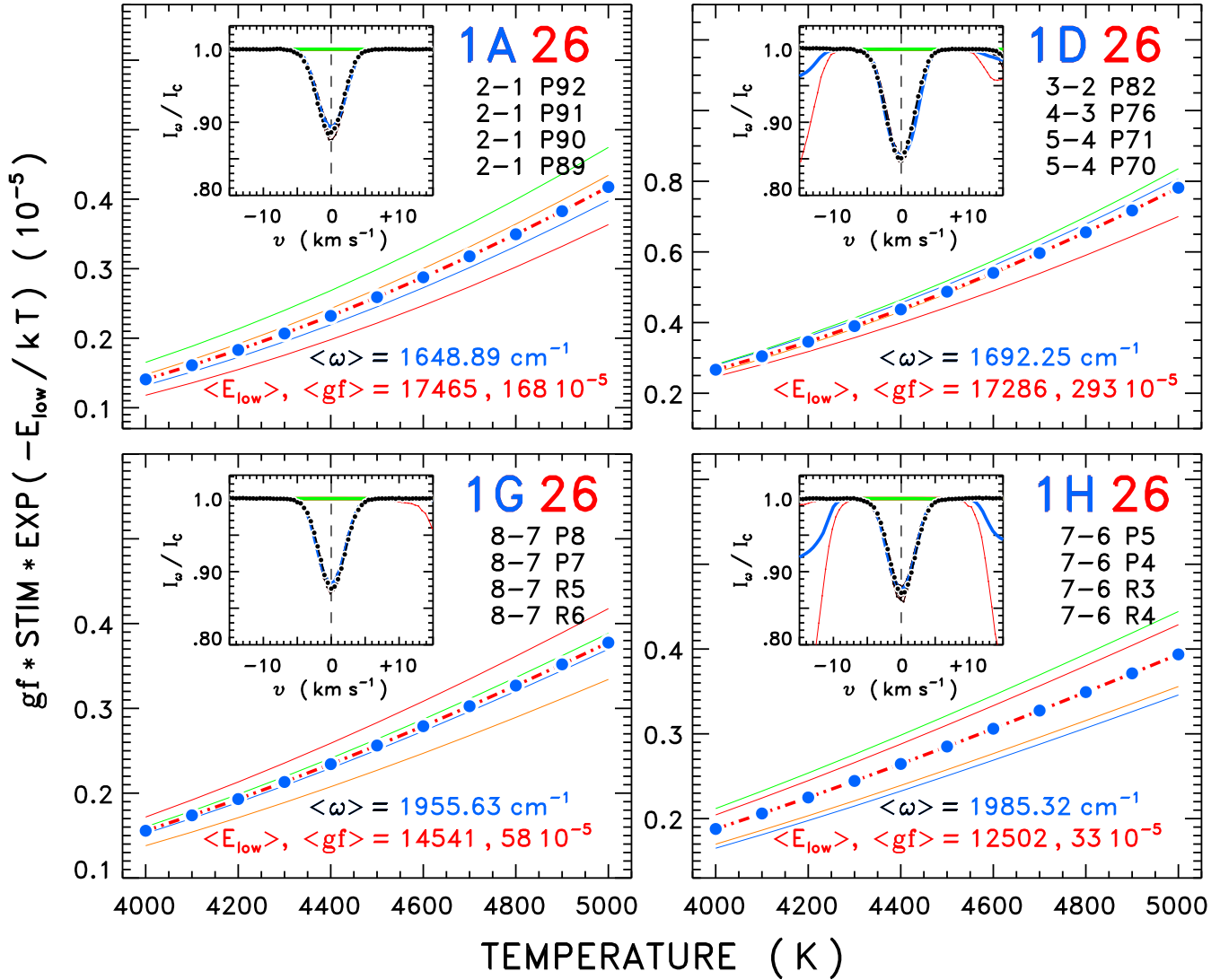


Fig. 2a.—

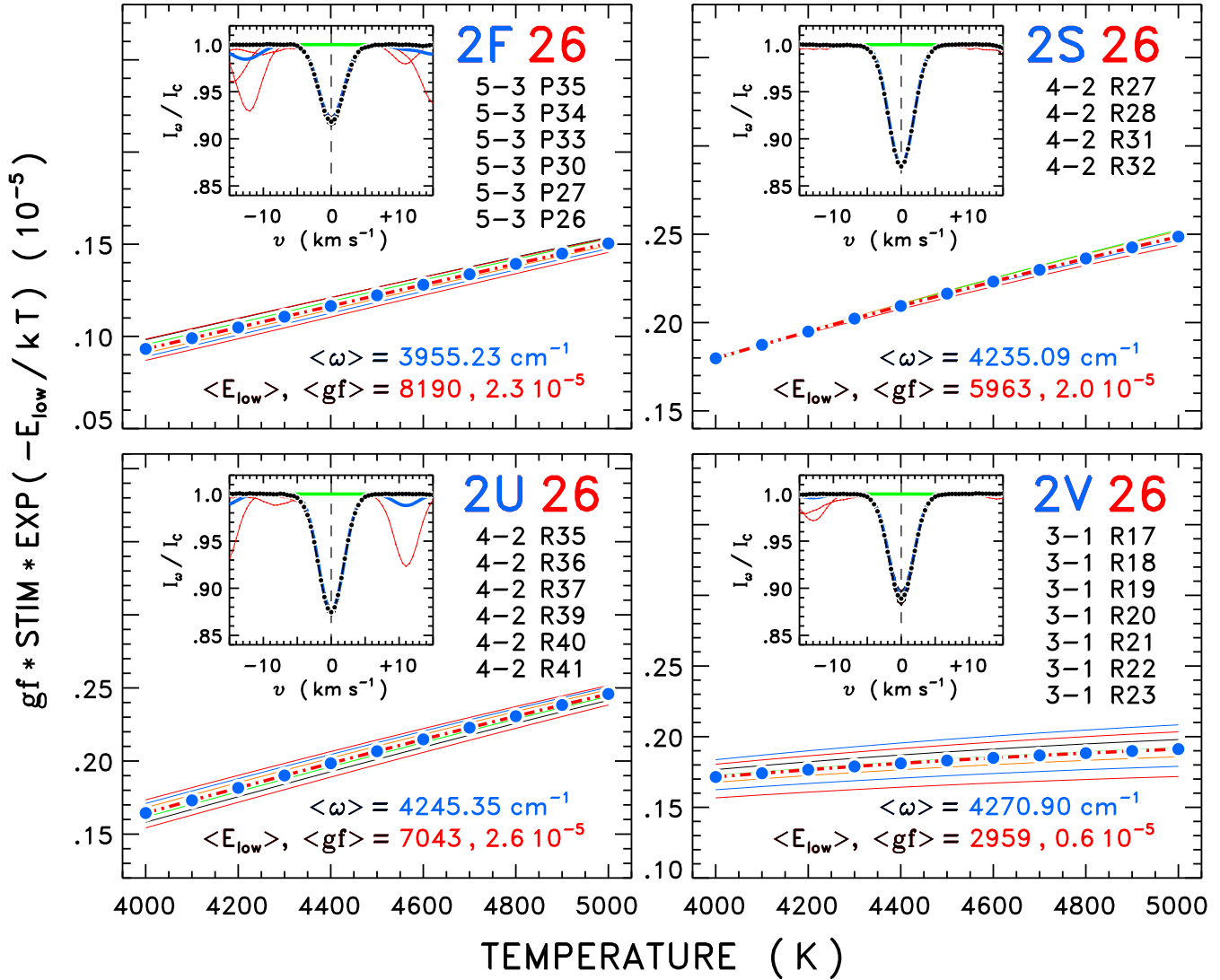


Fig. 2b.—

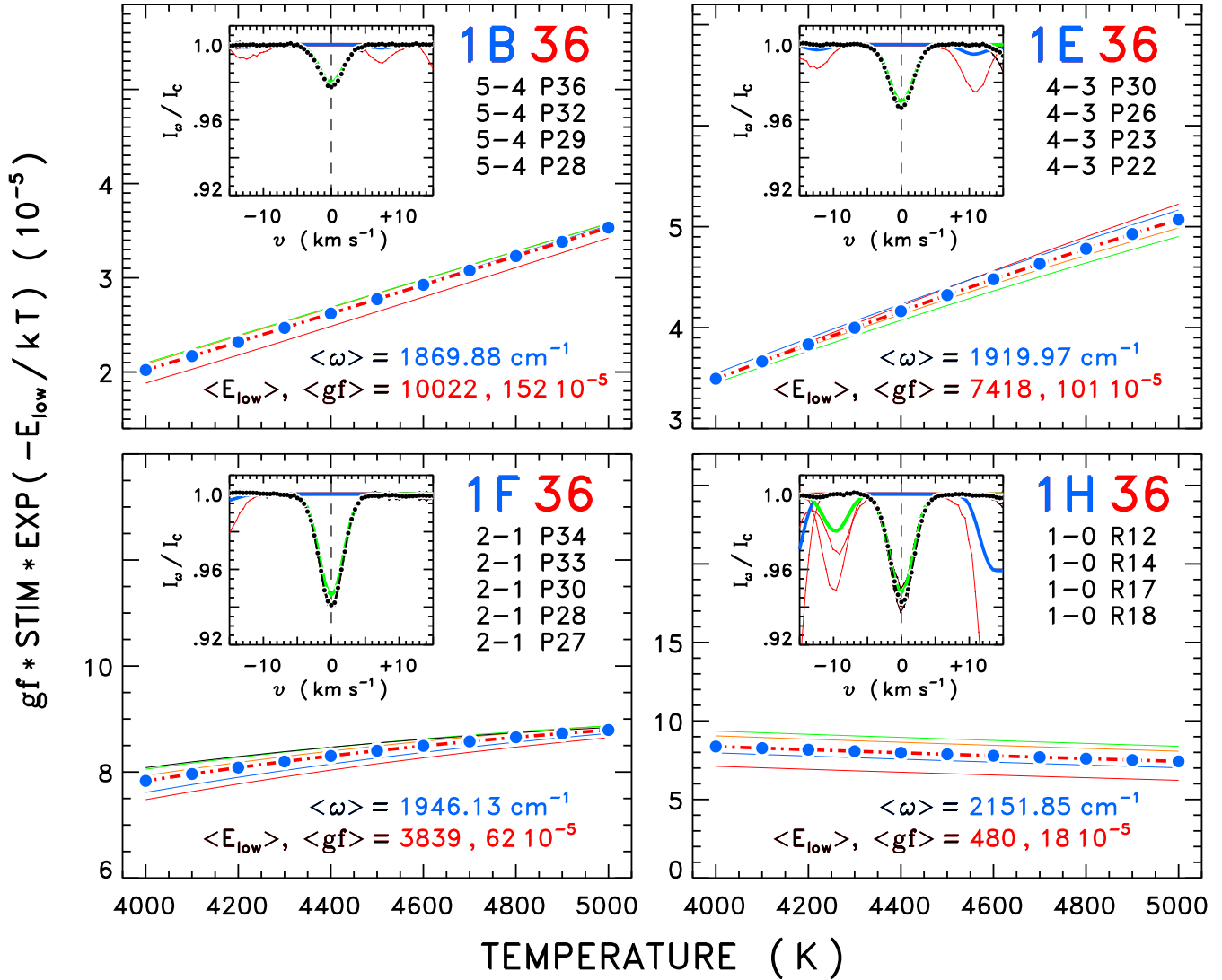


Fig. 2c.—

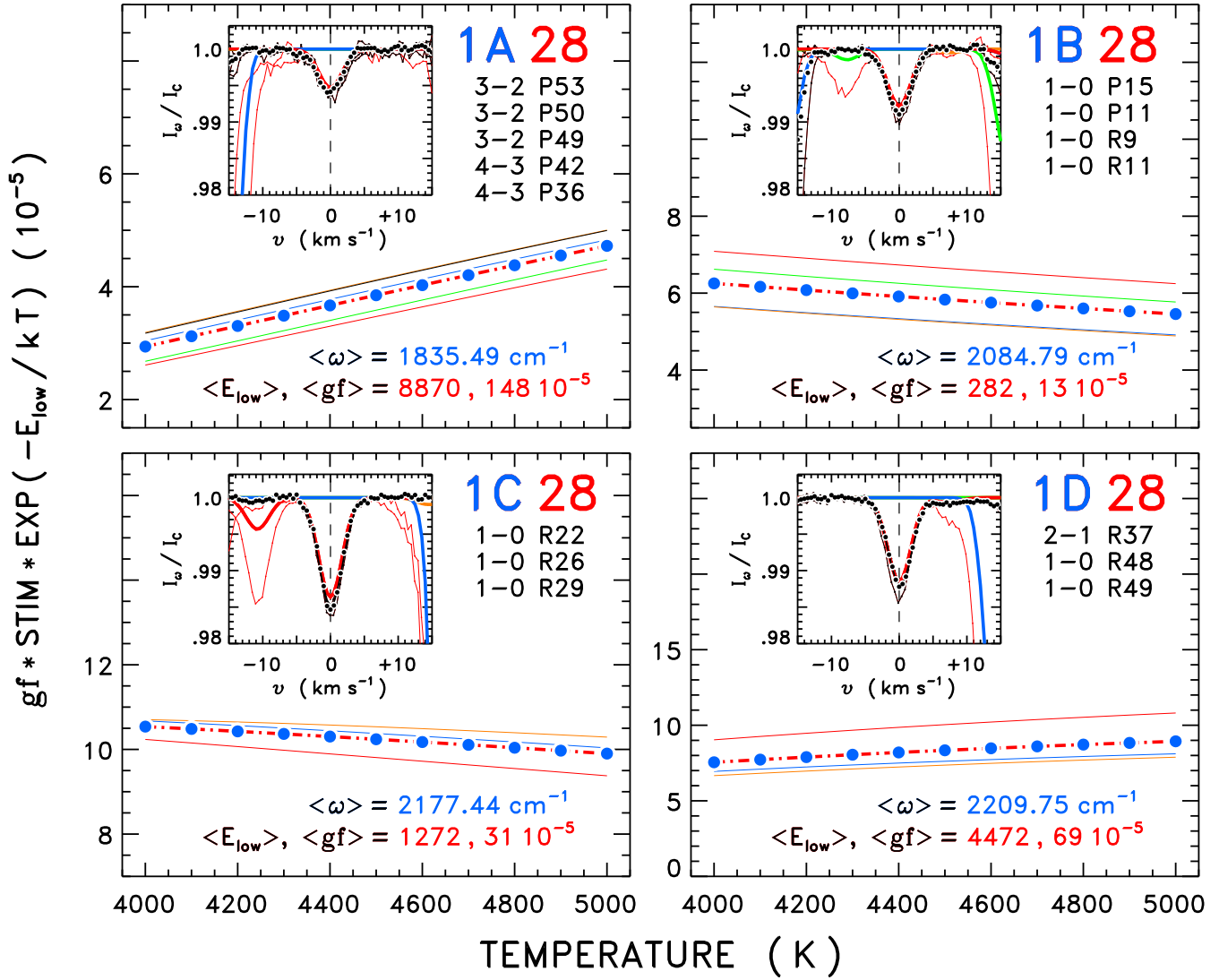


Fig. 2d.—

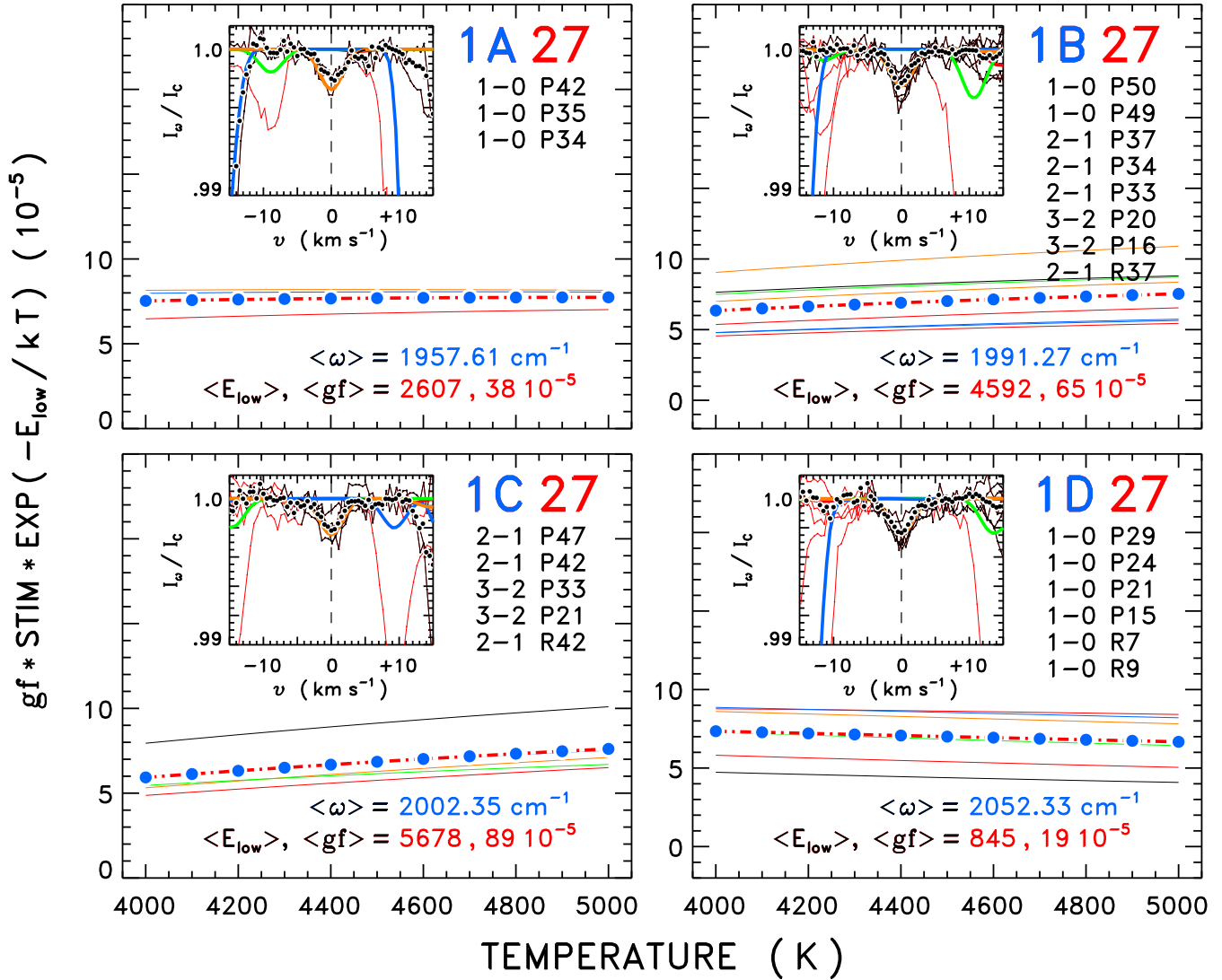


Fig. 2e.—

Fig. 3.— (a) Schematic maps of velocity (left) and temperature (right) for sixteen CO5BOLD snapshots utilized in this study. Cuts are at constant height (median of $\log p = 5$ pressure surface). In the velocity map, lighter areas are upflows and darker areas are downflows, and red ticks indicate horizontal velocity components. The gray scale saturates at $\pm 2 \text{ km s}^{-1}$. In the temperature map, lighter areas are warmer and darker areas are cooler. The gray scale covers the range 5000–7000 K. Three snapshots highlighted in yellow were considered separately, and in more detail, to gauge systematic errors in the isotopic analysis. (b) Left panel depicts probability density map of temperature as a function of pressure from the full 3D model. Dashed blue curve is mean temperature profile (averaged over constant pressure surfaces). Right panel compares mean $T(p)$ (again blue dashed) with FAL-C semi-empirical 1D model (black dot-dashed). Thick red dashed profile was obtained by shifting temperatures of the 3D model uniformly by 90 K in the outer layers (“MAX” scenario), so that the mean stratification matched the 1D model in the middle photosphere where the CO molecules are most abundant. Boosting function is depicted, exaggerated, in upper part of the panel. Large dots indicate average pressures of continuum optical depth unity calculated with the full 3D model for $0.5 \mu\text{m}$ (green: visible), $2.3 \mu\text{m}$ (orange: CO $\Delta v = 2$), and $4.6 \mu\text{m}$ (red: CO $\Delta v = 1$). Shaded areas are relative CO number densities for the 1D model (black), baseline 3D snapshot (blue), and MAX modified 3D model (red) calculated using the same $\epsilon_{\text{O}} = 600 \text{ ppm}$. Even though the mean temperature profiles of 3D MAX and 1D FAL-C are similar, the former apparently can produce substantially more CO, thanks to the large 3D fluctuations acting on the strong low-temperature bias of molecular formation. Also note that the IR continua arise in deeper layers than where the bulk of CO resides.

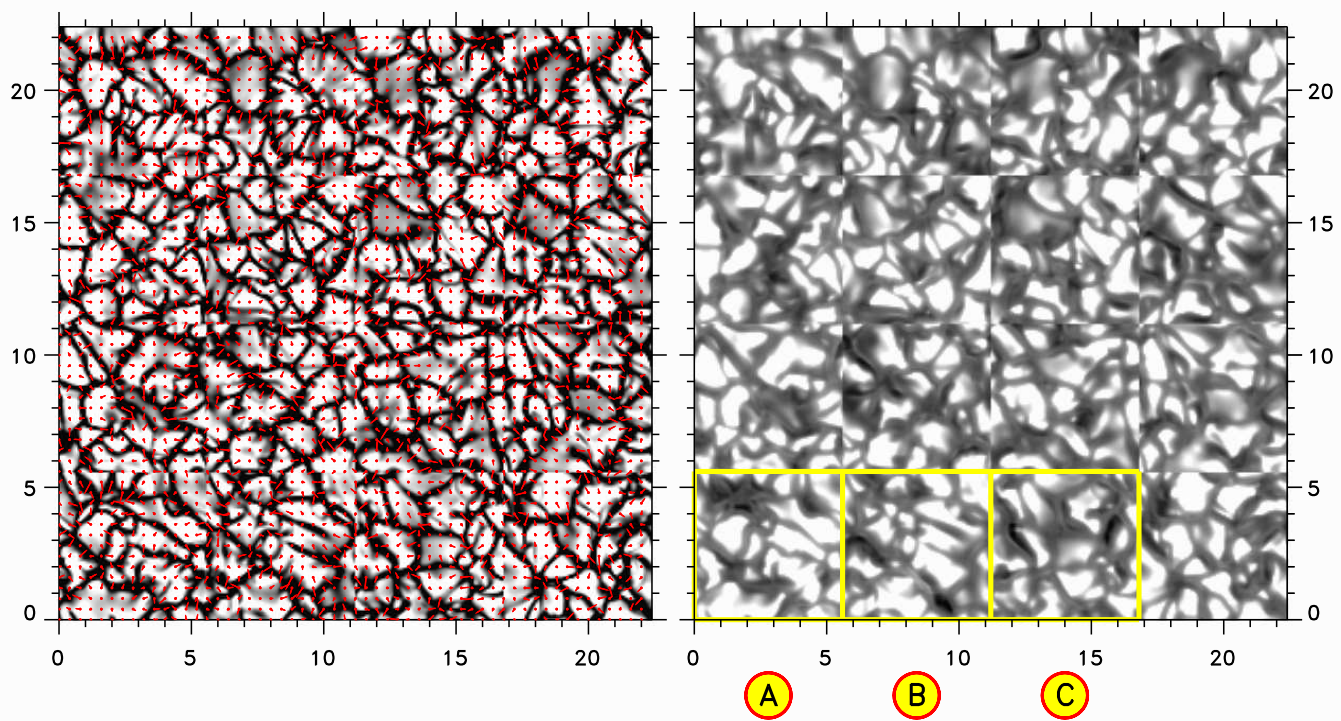


Fig. 3a.—

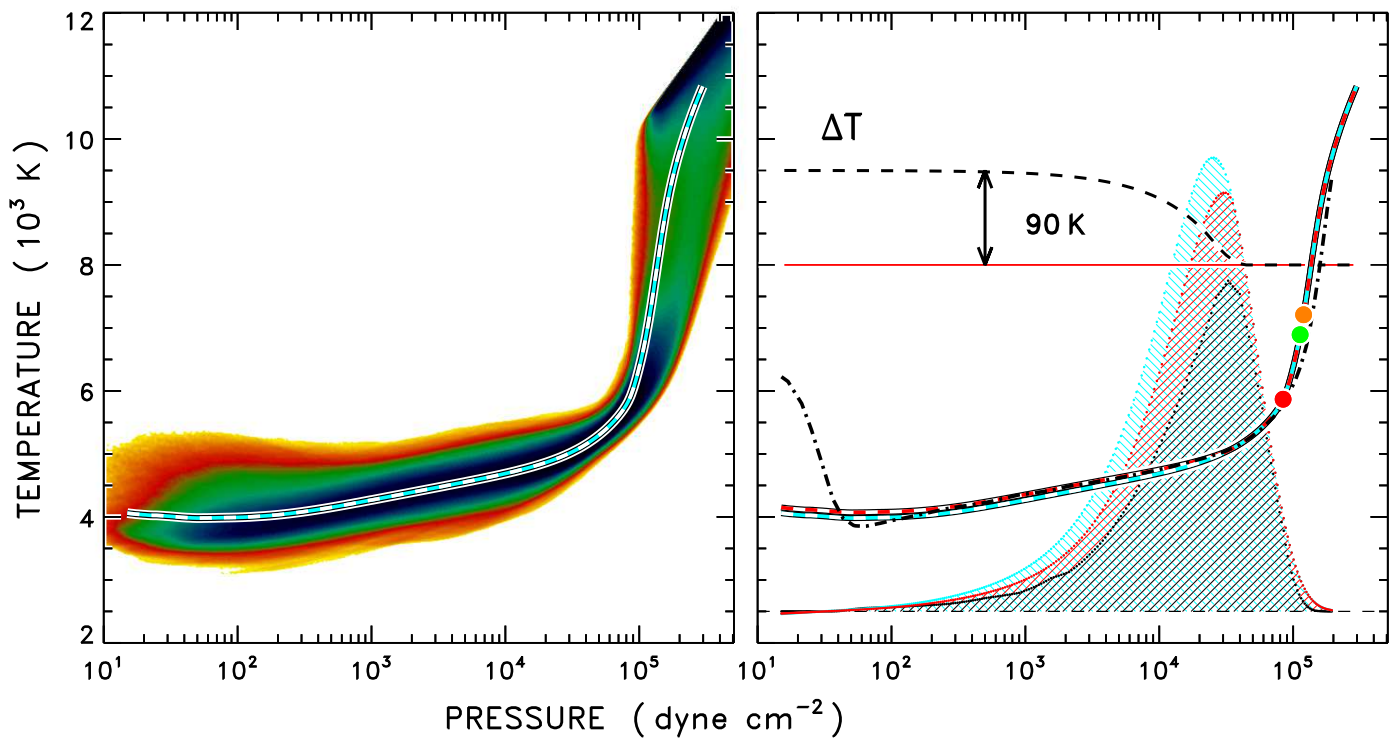


Fig. 3b.—

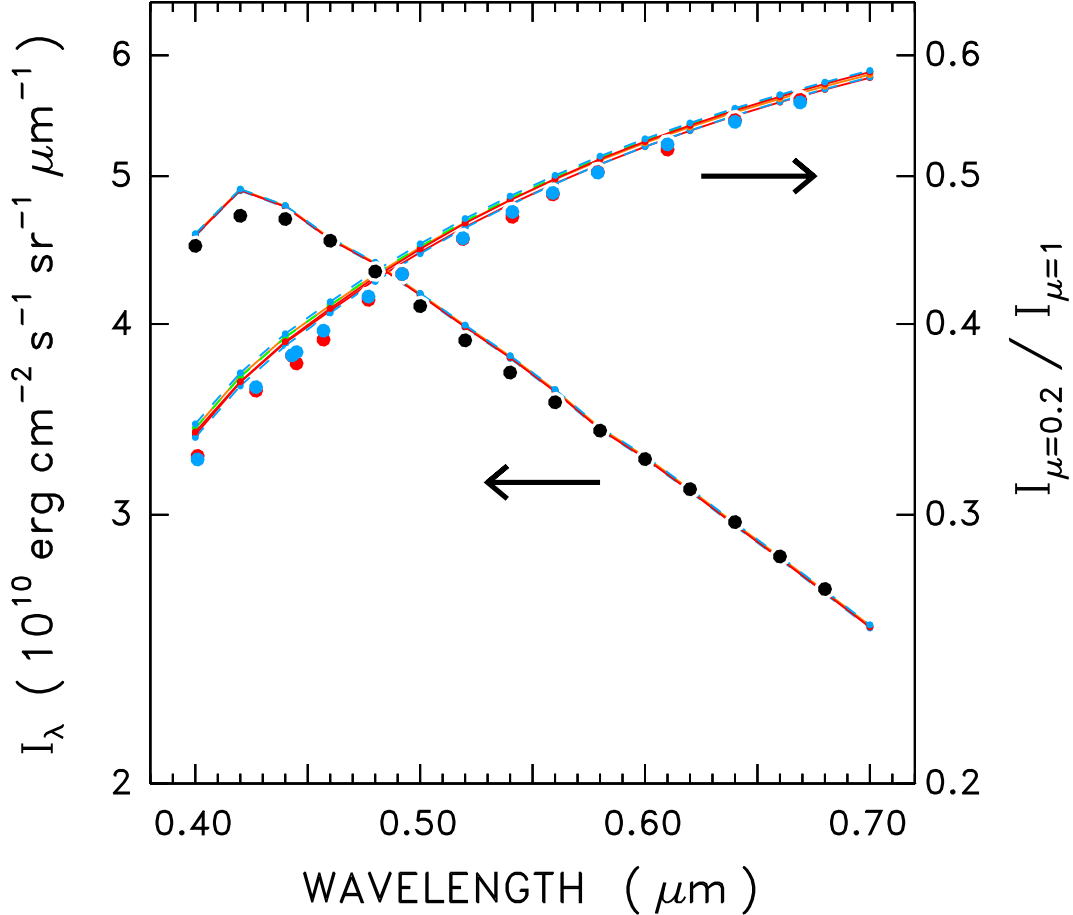


Fig. 4.— Comparison of absolute continuum intensities (left hand scale) and center-to-limb behavior (right hand scale: $\mu = 0.2$) at visible wavelengths predicted by the three baseline 3D snapshots, and their MAX counterparts. This is a fundamental consistency test for a model that seeks to mimic the solar photosphere. Large dots refer to measurements (two independent sets for the limb ratios); curves (and smaller dots) to simulations. Observational uncertainties are comparable to the symbol sizes. Baseline continuum intensities differ slightly from each other (although too small to be seen at this scale), owing to the stochastic nature of the convective process when viewed over the snapshot-size spatial area, but average is very close (actually 0.6–0.9% higher, by chance, for the three reference snapshots) to observed intensities (by design: the full 3D model was adjusted slightly in pressure to force agreement with these absolute measurements). The MAX perturbed cases also fall on top of the baseline models (the temperature enhancement is too shallow to affect the deep-seated visible continuum). There is more of a separation in the center-to-limb curves, with the baseline models predicting the lower curves (better matches to observations), while MAX models predict slightly higher limb intensities.

Fig. 5.— (a) Montage of $^{12}\text{C}^{16}\text{O}$ hybrid profiles (larger dark dots) and synthesized line shapes (smaller red dots: smooth curves are Gaussian fits) for full 3D baseline model and four values of the oxygen abundance. Average of G94 and HR96 oscillator strengths was used. Line designator and isotopomer (all are 26 here) are listed in upper part of each panel; line $\langle \omega \rangle$ and E_{low} (both in cm^{-1}) are listed below each panel. Note slight convective blueshift of each line (amounting to about 300 m s^{-1} for $\Delta v = 1$, and about 380 m s^{-1} for $\Delta v = 2$). (b) Calculated equivalent widths of hybrid lines of (a) for the four discrete oxygen abundances. Curves are parabolic fits to the points; horizontal lines indicate observed W_ω (error bars too small to be seen). Vertical ticks mark ϵ_{O} 's that correspond to observed W_ω 's. (c) Oxygen abundances of (b) as functions of E_{low} (upper panel) and W_ω (lower panel), separated by Δv : the more numerous overtone transitions are blue symbols; fundamental lines are red. Full 3D baseline model occupies lower part of each panel, while upper points are for 1D FAL-C. Green dashed lines are least-squares fits to the overtone sample; orange dashed lines are a forced fit to the sparser fundamental sample, with same slope. For the 3D model, $\epsilon_{\text{O}} = 572 + 7(E_{\text{low}}/10^4)$ from first-overtone lines, and $\rho = 0.972 \pm 0.013$ is the offset of fundamental relative to first overtone. Note that the $\epsilon_{\text{O}}/E_{\text{low}}$ slopes are very different in 1D and 3D, and the 1D model yields much higher derived oxygen abundances. In the lower panel, lack of conspicuous trends between derived 3D ϵ_{O} and W_ω suggests that the sample has successfully avoided saturation effects. (d) Similar to (c), but now on an expanded ϵ_{O} scale and including MAX (small squares and orange lines) and Goldilocks ($\rho \equiv 1$: large diamonds and black lines) temperature enhanced versions of baseline snapshot, again using the $\langle f \rangle$ scale.

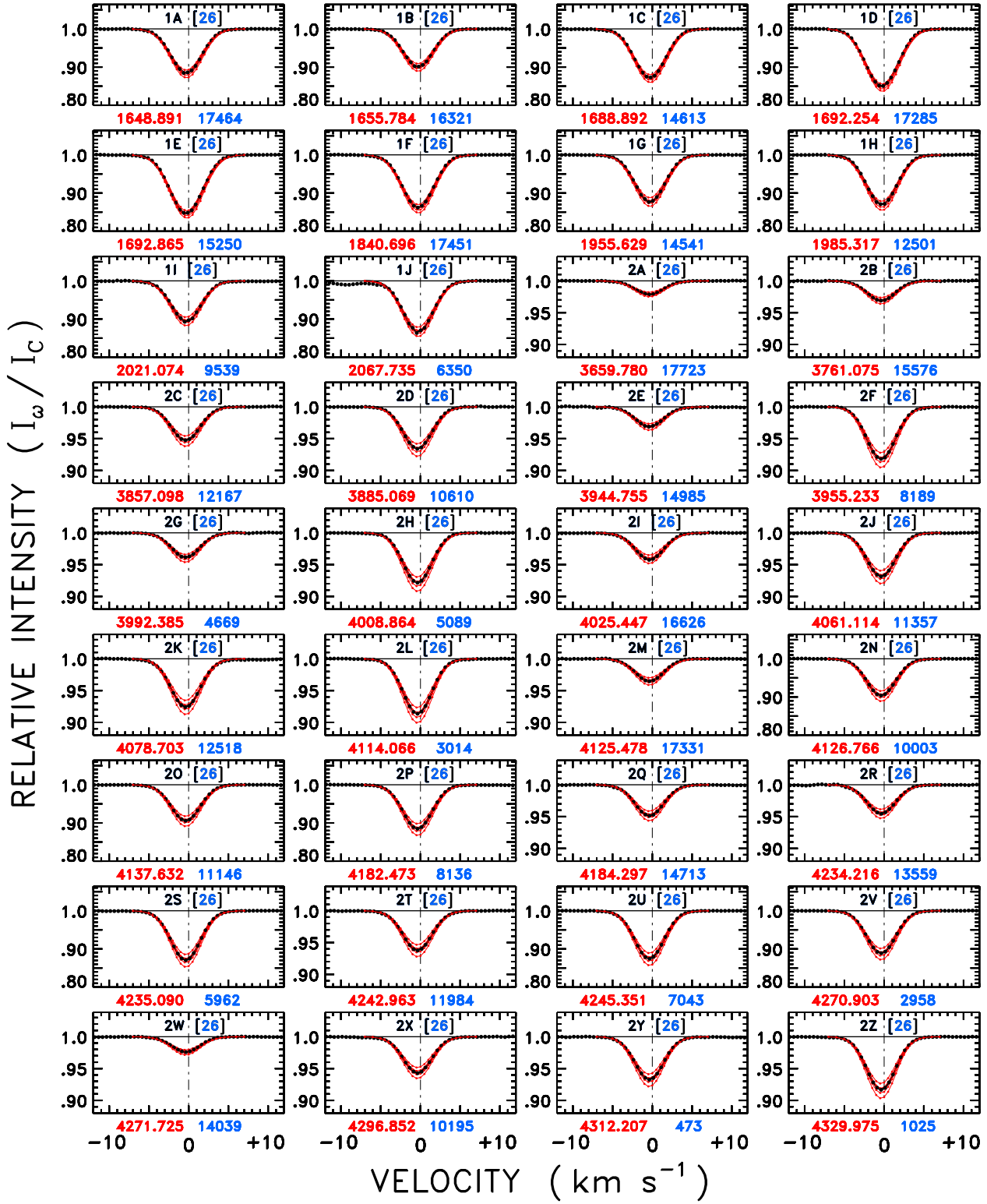


Fig. 5a.—

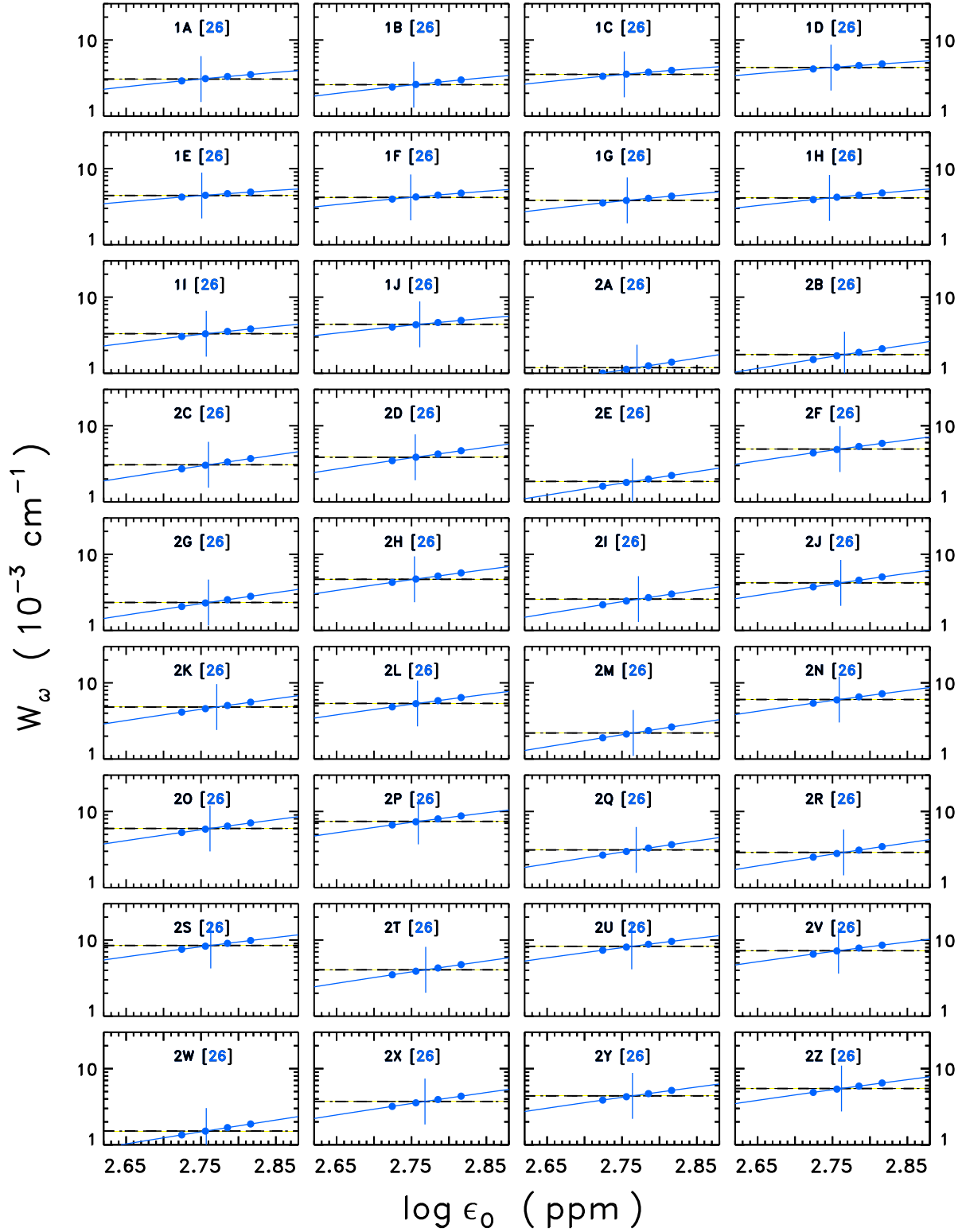


Fig. 5b.—

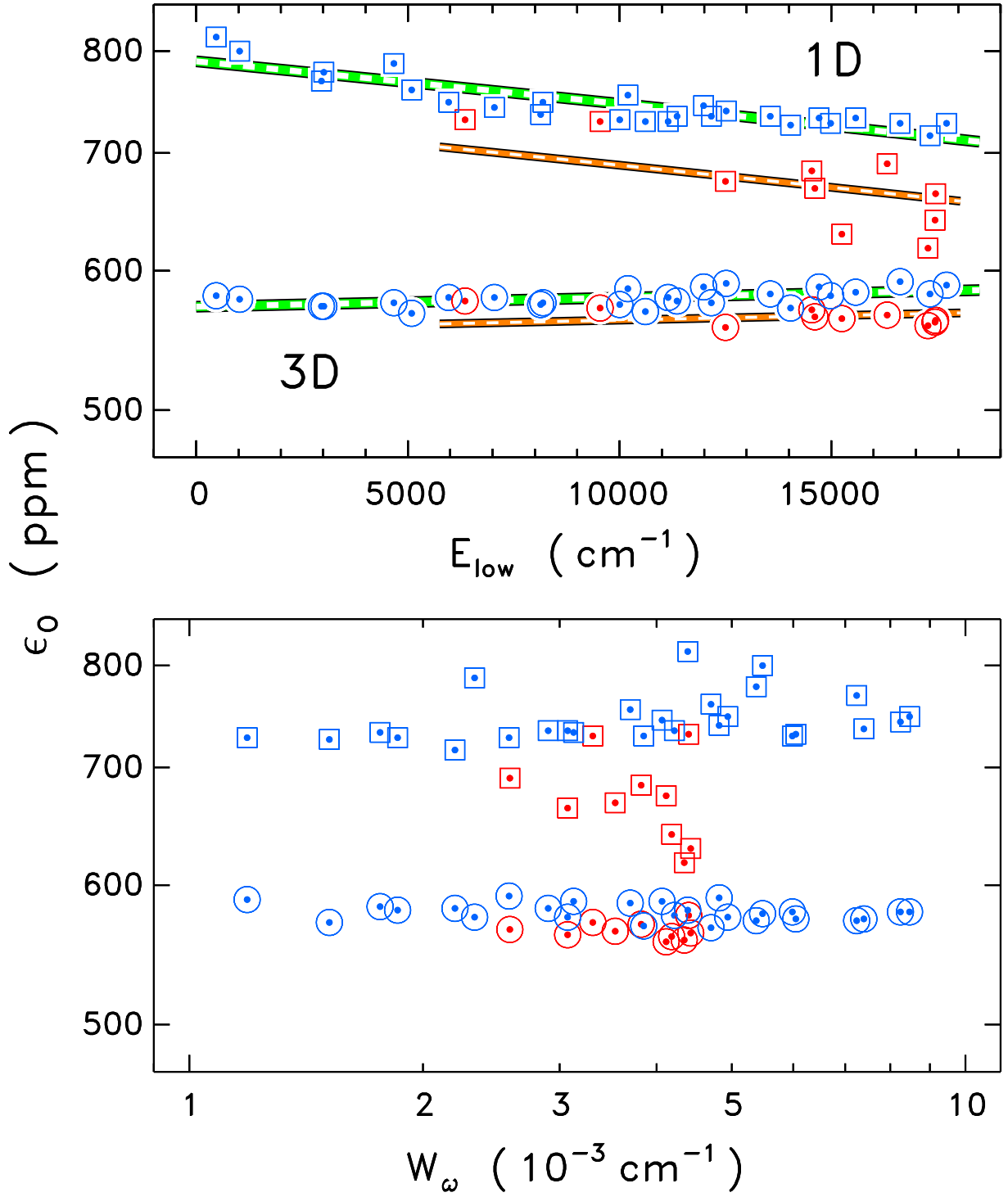


Fig. 5c.—

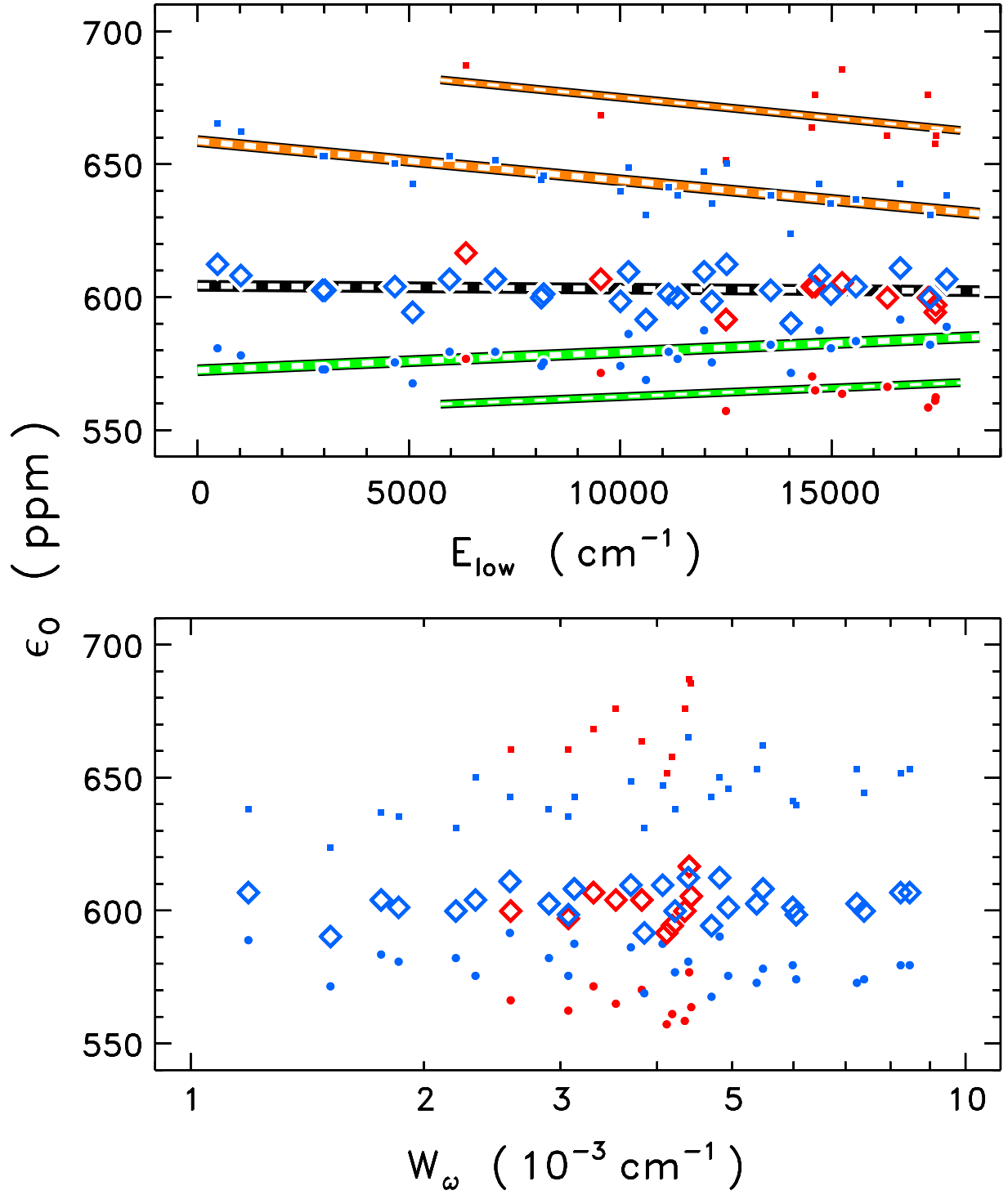


Fig. 5d.—

Fig. 6.— Summary of 3D abundance experiments utilizing the parent hybrid sample. Derived oxygen abundances on y -axis are compared to $\epsilon_{\text{O}}/E_{\text{low}}$ slopes on x -axis. “Bow-tie” symbols each refer to one of the three reference 3D snapshots (white shading for G94 f -values, green for HR96); or full 3D model, in yellow for the average f -values. Right edge of the bow-tie is for the baseline model: bottom value is $\Delta v = 1$ (marked by red dot); top value is $\Delta v = 2$. Left edge represents MAX-perturbed models: higher ϵ_{O} , and $\Delta v = 1$ values now above $\Delta v = 2$. Center of bow-tie is for Goldilocks option, where $\Delta v = 1$ and 2 coincide. FAL-C 1D model is represented by an analogous figure (yellow shaded for the $\langle f \rangle$ scale), although only a triangle because the MAX option is the 1D baseline model by definition. Lower dark hatched area indicates currently recommended oxygen abundance of Grevesse et al. (2010: GASS); upper thinner hatched zone is “seismic” value preferred by solar interior modelers (thick dashed line was derived from the favored metallicity Z parsed into an ϵ_{O} according to Grevesse & Savaul [1998] relative abundances; lower edge of hatched zone results if GASS abundance ratios are used instead). Intermediate red shading refers to Caffau et al. (2008) determination from atomic oxygen lines.

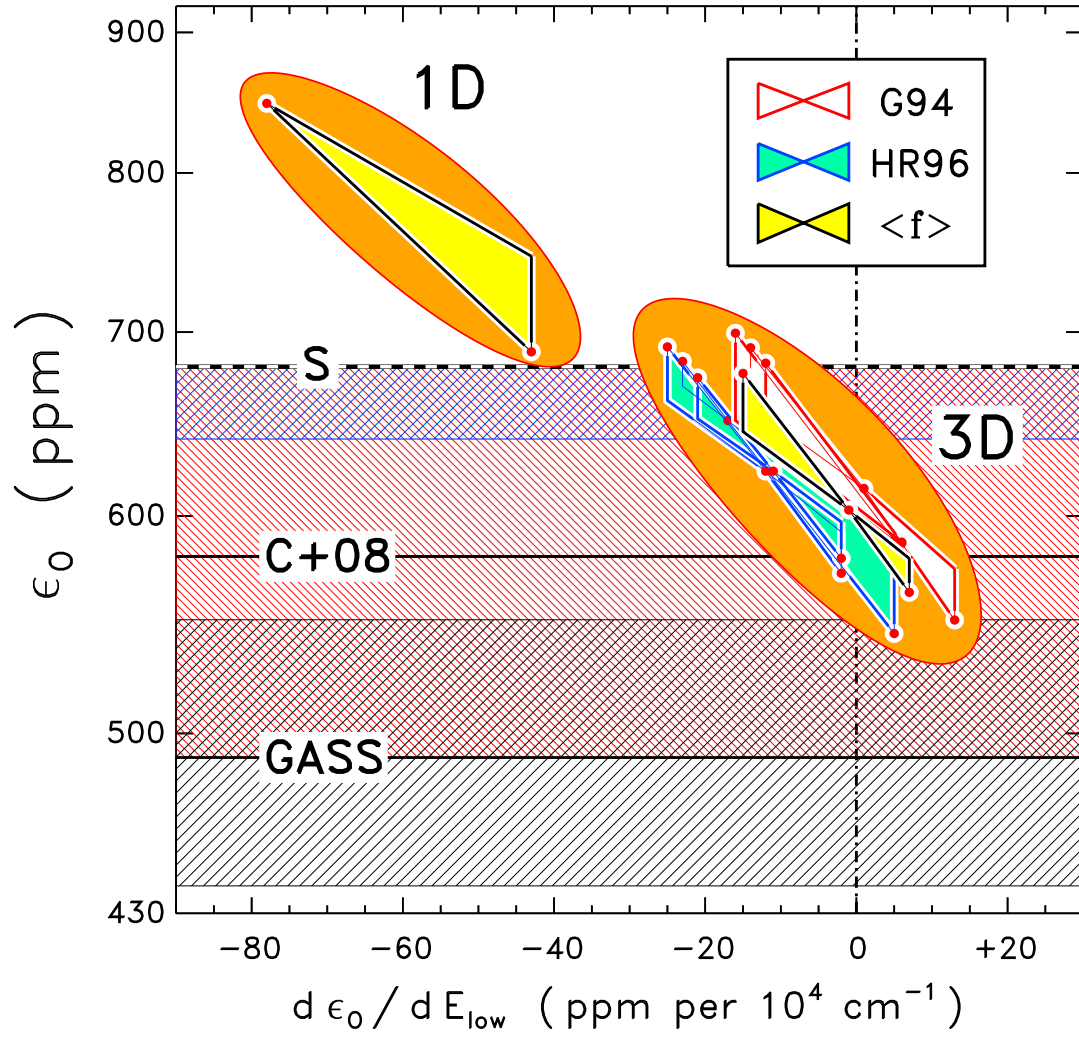


Fig. 7.— (a) Similar to Fig. 5a, but now montage of isotopomer hybrid profiles compared to synthesized line shapes for six multiples of standard isotopic ratios, assuming the $\langle f \rangle$ scale. (b) Similar to Fig. 5b, to derive individual isotopic ratio scale factors, relative to adopted standard $(R_{\text{ISO}})_{\text{STD}}$ values, from observed isotopomer W_ω . Widths of the horizontal lines $[(W_\omega)_{\text{obs}}]$ reflect measurement errors (only visible, and then just barely, for isotopomer 27). (c) Similar to Fig. 5c, but now showing the derived scale factors for the three isotopic combinations: 23 (red), 68 (blue), and 67 (green). The 23 and 68 values are tightly clustered about the means (solid lines), with small s.e.’s (dot-dashed lines); 67 displays larger spread consistent with its much smaller, and therefore less certain, equivalent widths.

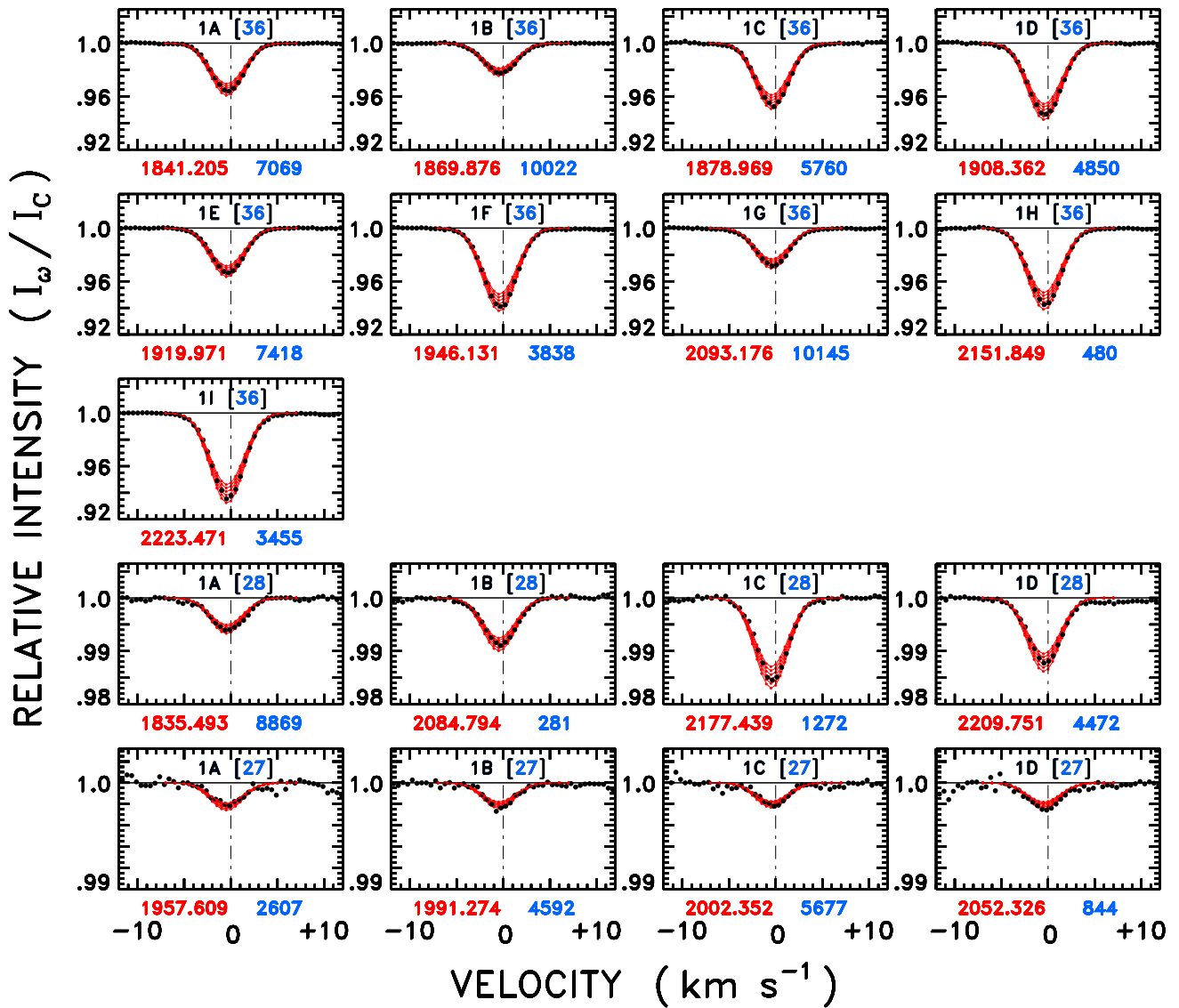


Fig. 7a.—

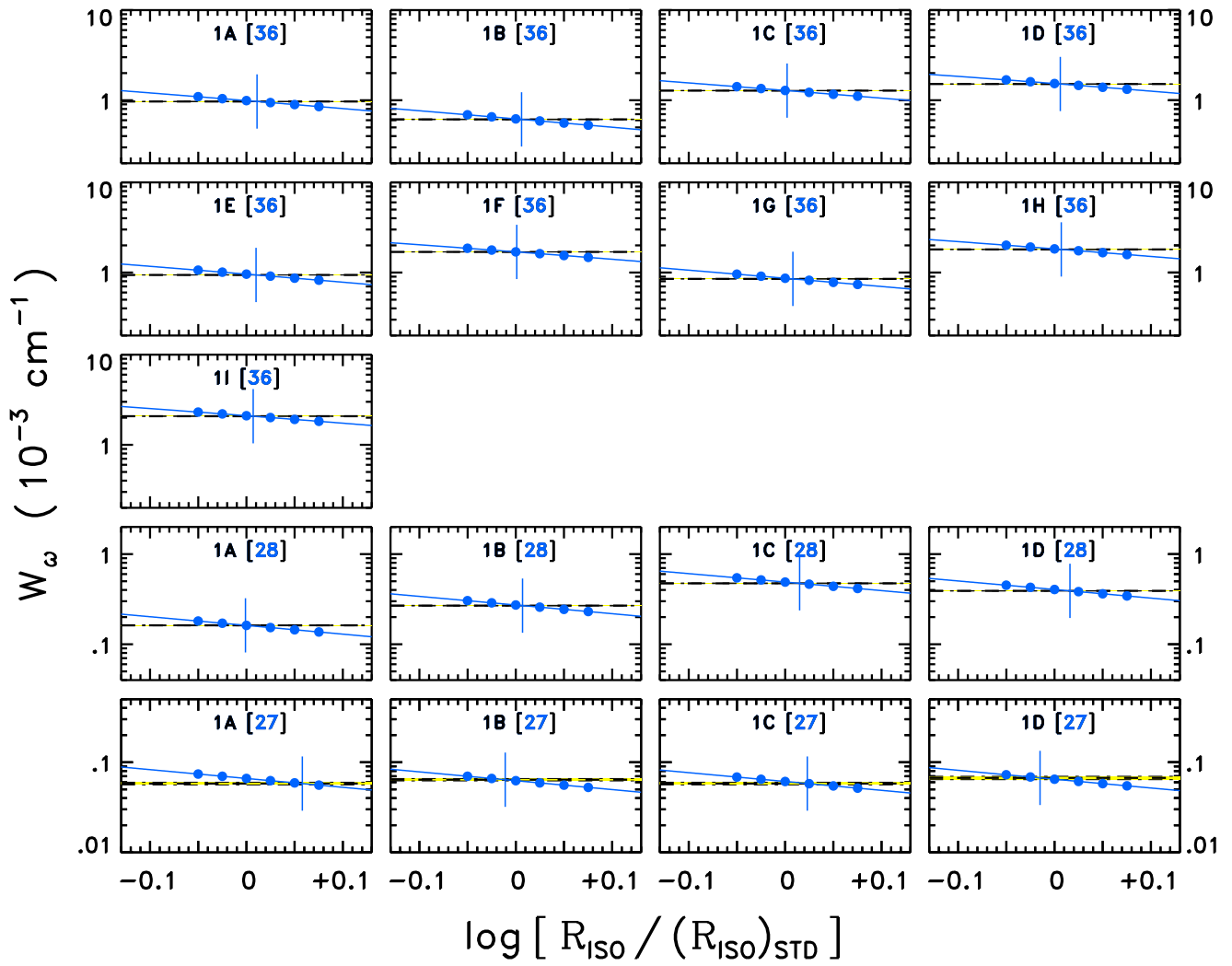


Fig. 7b.—

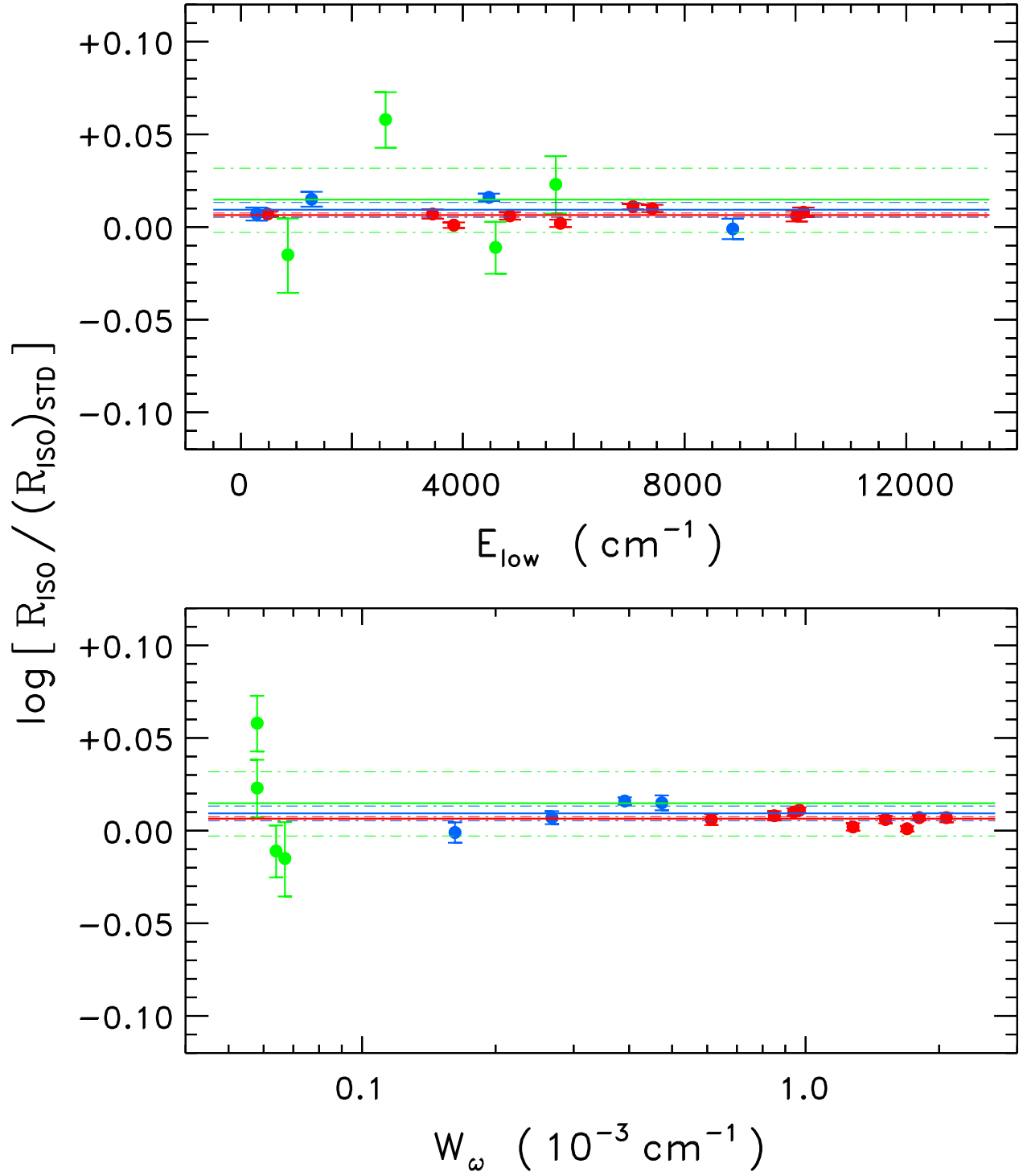


Fig. 7c.—

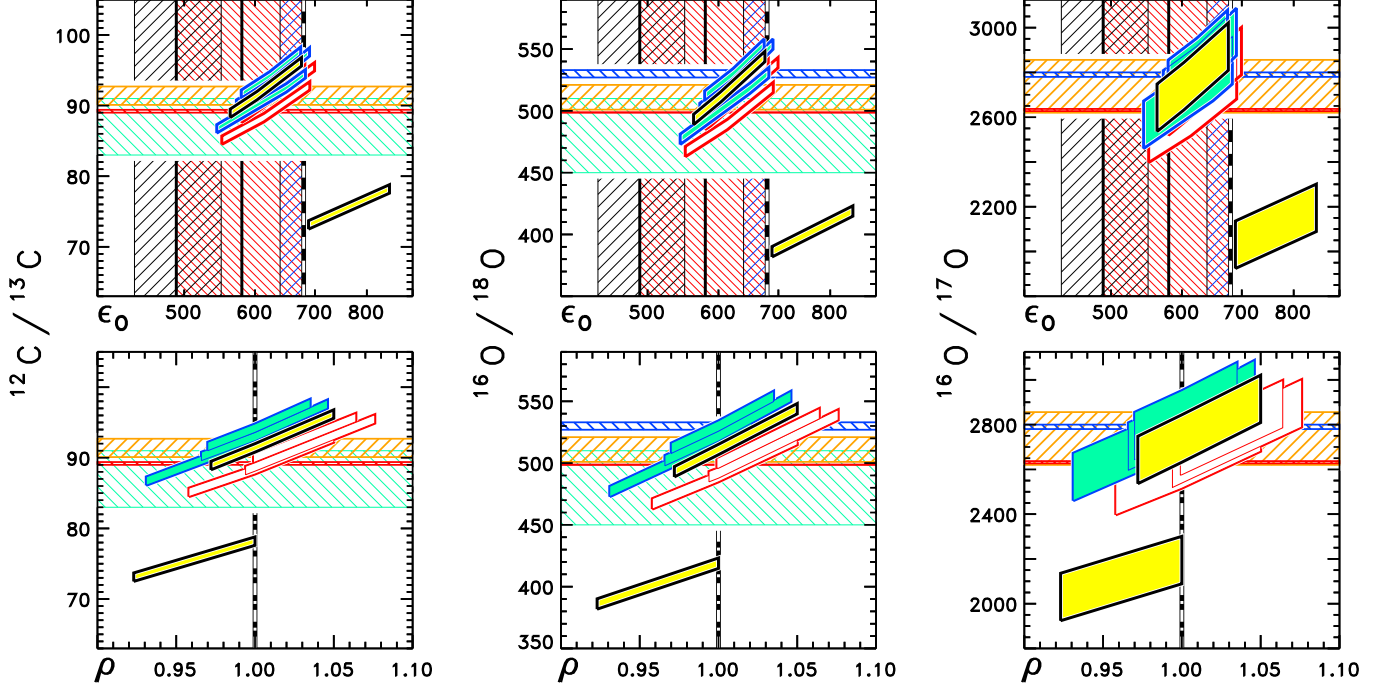


Fig. 8.— Summary of isotopomer experiments. Derived isotopic ratios are illustrated versus ϵ_O (from $\Delta v = 1$ sample) in upper panels, and versus the ρ value in lower panels. Included are the three reference snapshots, and the three temperature perturbation scenarios for each snapshot, for both the G94 (white/red) and HR96 (blue/green) f -value scales; the full 3D model and its three scenarios, for the average f -values (yellow/black); and the FAL-C 1D model, also for the $\langle f \rangle$ scale. The scenarios define quasi-rectangular areas: vertical extent is average 1 s.e. statistical measurement error due to the hybrid sample. Baseline models are at lower left edges; MAX variants are at upper right edges; Goldilocks in the middle (or closer to the left for two of the G94 snapshots). Thin red horizontal hatched lines refer to terrestrial standard values; upper blue lines are for *Genesis* oxygen ($\delta \sim -60\text{‰}$); intermediate orange hatched areas are our preferred Goldilocks results based on the $\langle f \rangle$ scale, and with “optimistic” error bars; and green shading indicates the earlier 3D results of SAGS for ^{13}C and ^{18}O . Vertical shaded bands in the upper panels refer to the same oxygen abundance ranges illustrated in Fig. 6.